RICE UNIVERSITY

ELECTRONIC CHARGE INJECTION AND TRANSPORT
IN ORGANIC FIELD-EFFECT TRANSISTORS

by

Behrang Homayoun Hamadani

DOCTOR OF PHILOSOPHY

HOUSTON, TEXAS

January 2007

RICE UNIVERSITY

Electronic Charge Injection and Transport
in Organic Field-Effect Transistors

by

Behrang Homayoun Hamadani

A THESIS SUBMITTED
IN PARTIAL FULFILLMENT OF THE
REQUIREMENTS FOR THE DEGREE

Doctor of Philosophy

APPROVED, THESIS COMMITTEE:

Douglas Natelson, Chair
Associate Professor of Physics and Astronomy
and Electrical and Computer Engineering

Peter J. Nordlander
Professor of Physics and Astronomy and
Electrical and Computer Engineering

Daniel M. Mittleman
Associate Professor of Electrical
and Computer Engineering

HOUSTON, TEXAS

January 2007

Abstract

ELECTRONIC CHARGE INJECTION AND TRANSPORT IN ORGANIC

FIELD-EFFECT TRANSISTORS

by

Behrang Homayoun Hamadani

Electronic devices based on organic semiconductors, such as field-effect transistors (FETs) and light emitting diodes have attracted much interest as possible inexpensive and flexible alternatives to inorganic devices. Despite considerable improvement in device properties, a better understanding of the nature of charge transport in these devices and the physics of contacts is crucial to further development of optoelectronic organic devices. This work outlines our findings in understanding and characterizing the injection and transport mechanisms of charge carriers in solution processed poly (3-hexylthiophene) (P3HT) field-effect devices. We measured hole transport in P3HT FETs with Au electrodes at sub-micron channel lengths as a function of gate voltage and a wide range of temperatures. The strongly nonlinear and gate modulated transport is shown to be consistent with a model of Poole-Frenkel-like hopping mechanism in the space-charge limited current regime. Charge injection from different source/drain electrodes such as Au, Cu and Cr was examined over a broad temperature range, and the contact current-voltage characteristics were extracted from the dependence of conductance on channel length. The differences between linear vs. nonlinear charge injection were carefully studied and compared to recently developed models of charge injection. In addition, the effect of doping-dependent charge injection in devices with Au and Pt contacts was studied, revealing large contact resistances and marked non-Ohmic transport at low dopant concentrations. Ultraviolet photoemission spectroscopy (UPS) reveals that metal/P3HT band alignment is rearranged as samples are dedoped, leading to an increased injection barrier for holes, with a greater shift for Au/P3HT. We also performed a study using dipole-containing self-assembled monolayers on the Au source and drain electrodes to strongly manipulate the charge injection process across the metal/organic interface. We have shown that chemically increasing the injecting electrode work function significantly improves hole injection relative to untreated Au electrodes.

Acknowledgments

First and foremost, I would like to thank my advisor, Prof. Douglas Natelson for his support, understanding and patience during the past five years over this project. Without his guidance as a great mentor, this work would not have been possible, and I certainly wouldn't be here. I would also like to thank Prof. Daniel Mittleman and Prof. Peter Nordlander for taking their valuable time and providing great input into this work.

Secondly, my special gratitude goes to my fellow lab mates, Dr. Lam Yu (now at NIST), Aaron Trionfi, who introduced me to Mathematica and helped greatly with programming issues, Sungbae (Jaylin) Lee, Zachary Keane and more recently Jeffrey Worne and Daniel Ward for the discussions, lab assistance and their support. I also thank our research collaborators, Huanjun Ding and Prof. Yongli Gao from the University of Rochester for the UPS measurements and David Corley, Dr. Jacob Ciszek and Prof. James Tour from the Chemistry Department for preparing the dipolar SAM molecules. A well deserved "thank you!" to my friend Hardin Dunham and his wife Angela for 5 years of unbroken friendship and support in the times that I needed it most. Special thanks to Dr. Leonard Suess for his friendship and many hours of enlightening conversation and support. I also thank my friend Pascal Mickelson for almost four years of exciting Wednesday-night racquetball games. Finally, my deep gratitude goes to John-David Rocha, Andrew Osgood, Erik Lotfi and all others who in one way or another further made my time at Rice worthwhile.

I am also greatly indebted to companionship of a small circle of close friends outside of Rice community who have continuously supported me throughout these years. I thank Bill and Martha McMullen for many years of true friendship, and for believing in me and encouraging me in this winding road. My sincere thanks goes to Shaadi Nezami, Encarna Bermejo and Darian Nezami (who calls me big brother) for always being there for me, and their kindness and the many memorable moments over the past 5 years. Finally, to Ramon Mourhatch, for 12 years of loyal friendship and all the unforgettable times we have spent together; thank you for giving me the honor of being your friend!

Without the love and support of my family, this would have been a very hard journey. I thank my father for teaching me good values such as hard work and appreciation for the gift of life and my mother without whom I would not be the person that I am today. My love for them is eternal. Finally, I am dedicating this work to my beautiful

Table of Contents

List of Figures

Chapter 1

INTRODUCTION

1.1 Organic Semiconductors

1.1.1 Introduction

Organic semiconducting materials have been synthesized and studied for over 5 decades [4]. In the 1950s, drift mobility measurements and the photoconductivity (PC) response of small molecules such as anthracene were examined [4, 5] and although these materials showed semiconducting properties (i. e., conductivities in the range of $10^{-9} - 10^{-6} Scm^{-1}$) [6], their performance and stability were poor. However, with drastic improvements in synthesis and processing of new classes of molecules such as conjugated polythiophenes in the past two decades [7], the prospects of commercially using organic semiconductors (OSCs) in applications such as organic light-emitting diodes (OLEDs), field-effect transistors (OFETs) and the solar cells is now greater than ever. In fact, in 2002 Philips introduced the *Sensotec Philishave* [1] as the first product in the market featuring a display panel based on OLED technology, and following suit, Kodak has introduced [1] the *Kodak EasyShare LS633* digital zoom camera with an award-winning OLED display technology (Fig. 1.1). Simplicity in manufacturing and lower costs of organic electronic devices have been cited [8, 7, 5] as the primary reasons for drive towards commercialization of these devices.

Figure 1.1: Two examples of use of OLEDs in commercial products. The image on the left shows a new Philips shaver (Sensotec Philishave) that was introduced to the market in 2002. It uses PolyLED technology for its display panel and was featured in the James Bond movie, Die Another Day. The image on the right shows the display of Kodak LS633 digital zoom camera driven by OLED technology. It allows for crisp and clear on-camera viewing of the images. Images taken from Ref. [1]

1.1.2 Conjugated materials

Today, conjugated materials are the most important class of organic semiconductors [9] and can be categorized into two main groups [6] of conjugated polymers and conjugated oligomers. Polymers, such as polythiophenes consist of many identical units bonded together in a long chain, and are macromolecular in nature, whereas oligomers like oligothiophenes consist of only a few units. In these materials, carbon p_z orbitals overlap and the π electrons become delocalized on the molecule, forming the so-called π-conjugated system [9, 8]. The alternating single and double bonds in polymer drawings represent these π electrons. There are other classes of π-conjugated OSCs, such as pentacene, fullerenes and etc. which have demonstrated good semiconducting properties. Fig. 1.2 shows some important organic semiconductors.

An important conjugated polymer, which has been our material of choice for all the
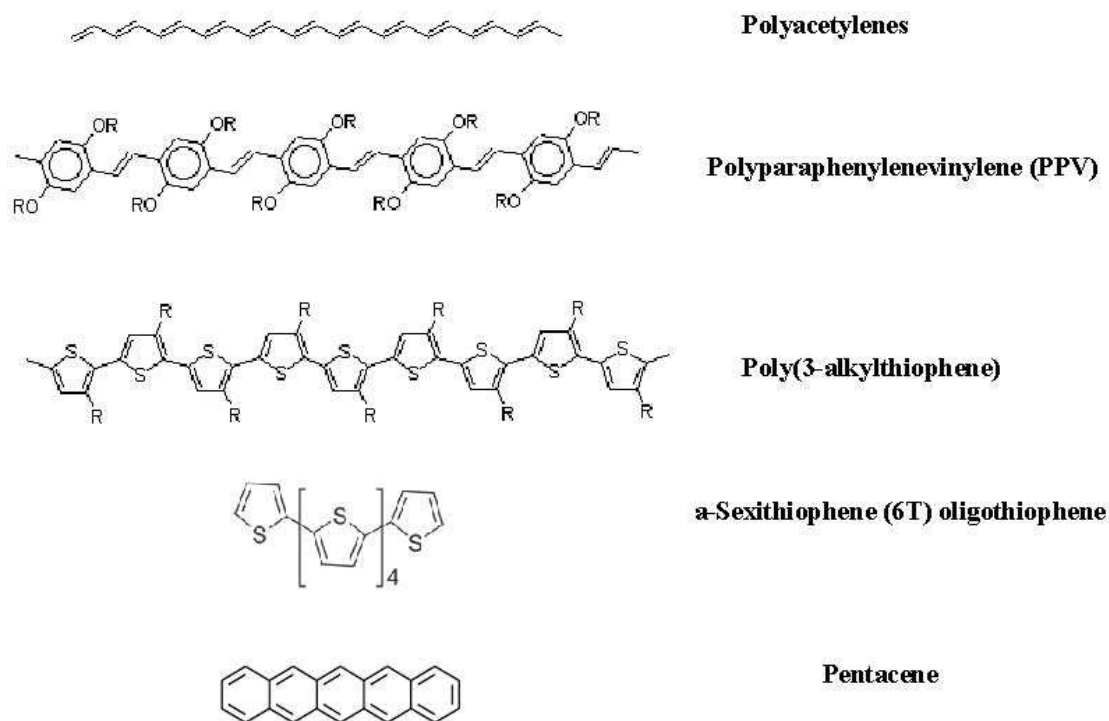
Figure 1.2: A few organic semiconductors. Images take from Ref. [2]

experiments and analysis presented in this thesis, is regioregular poly(3-hexylthiophene) (P3HT). Fig. 1.3 shows a sketch of this molecule. Regioregular means that each 3-hexylthiophene unit in the chain is oriented so that the residue group C_6H_{13} is either head to head or head to tail. This property gives the polymer, upon deposition, better self-organization and order, therefore, increasing substantially the device mobility [9]. Mobility, μ, which is usually reported in units of $cm^2/V.s$, is an intrinsic property of the material and is an indicator of how readily charge is transported within the semiconducting polymer upon application of an external electric field. For regioregular P3HT, we have
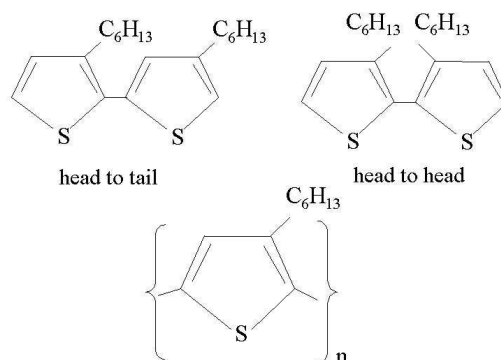
Figure 1.3: Poly (3-hexylthiophene) is an important OSC which is solution-processable and has demonstrated good semiconducting properties. P3HT has been the material of choice for the experiments outlined in this thesis.

commonly observed mobilities in the range of $0.1 - 0.3$ cm^2/V.s for field-effect transistors (see next section). This value is 5 orders of magnitude higher than those reported [7] for early polythiophenes over 15 years ago and is a testament of the ability in synthesizing new and improved organic semiconducting materials.

A variety of techniques have been employed to deposit organic semiconductors onto the active area of the device. One approach is to vacuum-deposit the polymer by thermal evaporation onto the substrate. Pentacene is a prime example of a small-molecule OSC which has confirmed high mobility and poly or mono-crystalline structure upon proper deposition conditions [8]. Another scheme to deposit OSCs is by processing from solution using printing, spin-coating or drop-casting. P3HT is an example of a polymer that is dissolved in a solvent such as chloroform and is deposited onto a pre-patterned array of electrodes. After the solvent is allowed to evaporate, a film of the polymer is left behind in the active area of the device. The films that are specially drop-cast from solution have

been shown [10] to form microcrystalline lamellar structures of 2-d conjugated layers allowing for effective charge transport parallel to the plane and resulting high mobilities.

1.1.3   Electronic structure of organic semiconductors

As in traditional inorganic semiconductors, the band gap between the highest occupied state (molecular orbital), HOMO, and the lowest unoccupied state (molecular orbital), LUMO, in OSCs is relatively small, typically between 1 to 4 eV [9]. Therefore, thermal excitation of electrons from HOMO to LUMO states is possible. However, due to weak Van der Waals forces between OSC molecules, the self-organization and band formation in these materials are poor. The existence of narrow bands and high degree of electron-phonon interaction and presence of disorder cause charges within the material to become confined in localized polaronic states shrouded by regions of molecular distortion [10]. In this case, charge transport occurs through thermally-assisted hopping or tunneling of carriers between adjacent localized states [11]. This is an activated process in nature and as we will see later, it has consequences for the temperature dependence of conductance in these materials.

1.2   Organic Field-Effect Transistors

1.2.1   Introduction

A field-effect transistor is a 3-terminal device configured like a parallel-plate capacitor. Fig. 1.4 shows a schematic view of a transistor. By controlling the voltage on one plate (the gate), a charge can be induced on the other. These charges are injected from the source electrode and collected across the conducting channel at the drain by applying a

voltage between the two [12]. A special type of transistor called the Metal Oxide Semiconductor Field-Effect Transistor (MOSFET) has become particularly important in modern electronic devices. Traditionally, silicon has been the most widely used semiconductor material. In addition to the great quality of Si-SiO$_2$ interface in MOSFETs, these devices exhibit fast switching speeds and are therefore suitable for use in modern processors [12].

There are however, many applications for field-effect devices where fast switching speed is not a requirement. These include [8] large-area coverage, mechanical flexibility and low cost integrated circuits. For example, amorphous Si FETs nowadays constitute the active matrix of liquid crystal displays [13] with the mobility in these devices being two orders of magnitude lower than their single crystal counterparts. With the successful synthesis of the first organic transistor in 1986 based on electrochemically grown polythiophene films [3], the prospect of replacing costly and labor-intensive inorganic devices with cheaper and more flexible organic electronic materials entered a new era. Over the past 15 years, we have seen dramatic improvements in growth, fabrication and processing of organic electronic materials and devices, placing them as good candidates for use in applications [8] such as electronic displays, smart cards and identification tags. A good example of this progress is a 5-order of magnitude increase in the field-effect mobility from 1986 to present [7], making the organic electronic devices a viable replacement for amorphous Si devices.

Despite considerable improvements in fabrication and characterization of thin-film organic field-effect transistors, the physics of charge injection and transport in these devices is not well understood. Before we discuss these issues in detail, a basic review of the transistor's mode of operation and the different charge injection mechanisms is

essential.

1.2.2   Operating mode

OFETs are generally prepared in two configurations: The bottom-contact and the top-contact. In the bottom-contact configuration shown in Fig. 1.4, first the gate electrode (a conductor) is prepared on a substrate. On top of the gate, a thin layer of a gate
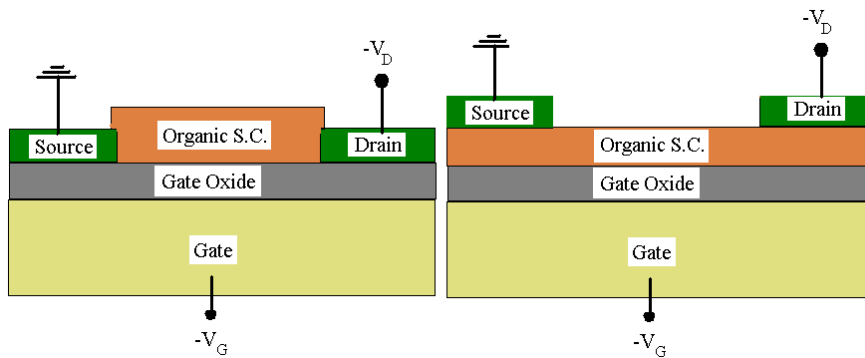
Figure 1.4: (left): A schematic view of a bottom contact OFET. The source electrode is grounded, while the drain and the gate are biased negatively. In this mode, holes are injected from the source and collected at the drain. (right): A top contact OFET with the electrodes patterned on top of the organic polymer.

insulator, usually an oxide such as SiO_2, is grown followed by the deposition of the metal source and drain electrodes. These electrodes are pre-fabricated on top of the oxide using lithography or shadow-mask techniques. Then the OSC material is deposited directly on top of the electrodes, filling the gap between them. This fabrication method is very suitable for large-area applications and nanometer-scale transistor design. In the top-contact configuration, the electrodes are patterned on top of the organic semiconductor. One advantage [14] of this configuration is the larger contact area between the electrodes and the OSC, as compared with the bottom-contact devices. This can allow for more

effective charge injection into the polymer. However, since patterning of the electrodes directly on top of the polymer is difficult and there is possibility of damage to the polymer film during the metal evaporation, the top-contact design is not used frequently.
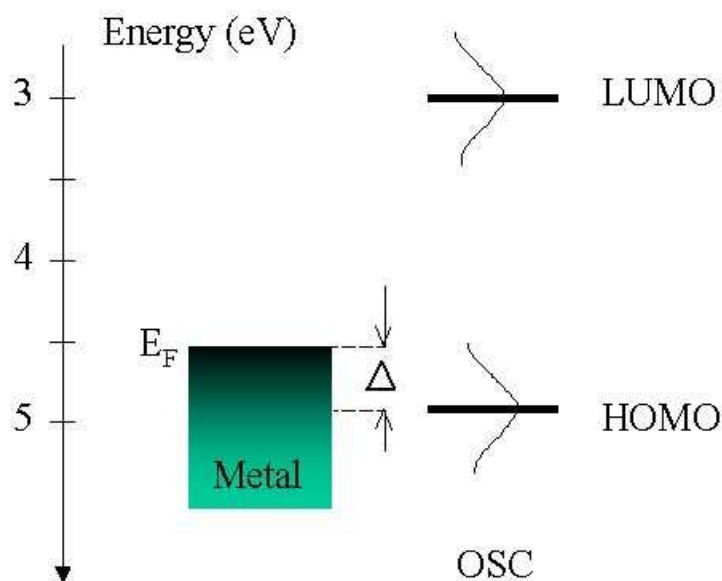
Figure 1.5: The energy diagram showing the band alignment at an OSC/metal interface such as Au/pentacene. Holes are injected from the Fermi level of the metal into a Gaussian energy-dependent state in the HOMO, overcoming an intrinsic energy barrier Δ (adapted from Ref. [3]).

Most OFETs reported in the literature so far show either p-type or n-type behavior, meaning that the charge carriers are either holes or electrons respectively. P-type OFETs comprise the majority of these devices, showing the best transport properties. However, very recently, a few groups [15, 16] have shown that ambipolar charge transport is also quite achievable and is a generic property of the OSCs. This can pave the way for fabrication of organic complimentary metal-oxide semiconductor (CMOS) logic circuits.

The OFETs work in accumulation mode. In hole transporting devices, a negative

voltage is applied to the gate, inducing holes at the source electrode. These positive

charge carriers will be injected into the OSC, provided that the hole injection barrier (Δ)

between the Fermi level of the metal and the highest occupied molecular orbital (HOMO)

of the OSC is low [3] (see Fig. 1.5) These accumulated holes form a conducting channel

at the OSC/insulator interface. By applying a second negative bias to the drain, the

charges move along the channel and are collected at the drain.
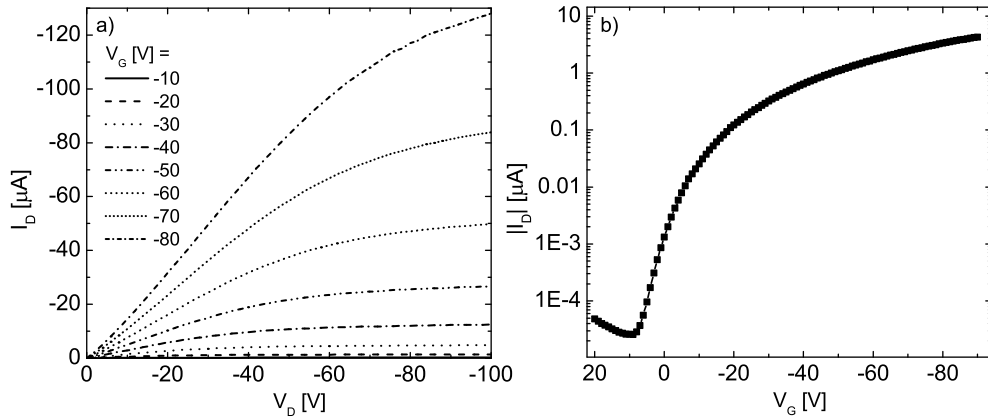
Figure 1.6: a: The output characteristics of a P3HT OFET with $W = 200\mu$m, $L = 5\mu$m, $C_i = 1.7 \times 10^{-4}$F/m^2 at room temperature. b: The transfer characteristic of the same device at fixed $V_D = -4$V.

1.2.3 Basic models

The operation of an OFET is defined by several parameters: the channel width (W)

which is the width of the source-drain region, the channel length (L) defined as the

spacing between the source and drain electrodes and the capacitance per unit area of the

gate insulator C_i. The current-voltage (IV) operation of a transistor is generally displayed

(Fig. 1.6a) by a plot of the drain current, I_D as a function of the source-drain voltage, V_D, at fixed gate voltages, V_G. This is called the output characteristic of a transistor. We can also plot I_D vs. V_G at a fixed drain bias as shown in Fig. 1.6b. This is the transfer characteristics and shows how effectively the gate voltage can switch the device ON or OFF. If a p-type transistor switches ON at $V_G > 0$, this could mean, among other things, that a significant density of impurity dopants is present in the semiconductor, constituting a bulk current, even when a gate voltage is not present [17].

At a fixed V_G, V_D initially increases linearly with I_D. The variation of I_D with the voltage in the channel at some position x can be written as [12]:

$$I_D = W C_i \mu [V_G - V_T - V(x)] \frac{dV}{dx} \qquad (1.2.1)$$

where V_T, the threshold voltage, is traditionally defined as the voltage below which the transistor is OFF on a plot of I_D vs. V_G, and μ is the intrinsic channel mobility of the charge carriers. Rewriting Eq. 1.2.1 as:

$$dx = [W C_i \mu (V_G - V_T - V(x)) dV] / I_D \qquad (1.2.2)$$

and integrating from 0 to L, we find:

$$I_D = \mu (W/L) C_i [(V_G - V_T) V_D - V_D^2 / 2] \quad \text{for } V_D \leqslant V_{Dsat} = V_G - V_T \qquad (1.2.3)$$

$$I_D = (1/2) \mu (W/L) C_i (V_G - V_T)^2 \quad \text{for } V_D \geqslant V_{Dsat} = V_G - V_T \qquad (1.2.4)$$

When the value of the drain voltage becomes comparable to the gate voltage (assuming V_T is small), I_D ceases to increase and the transistor enters the saturation regime. In the saturation, the channel is pinched off at the drain and the current levels off (see Fig. 1.6).

An important parameter in the operation of a transistor is its field-effect mobility, μ. In the linear regime, it can be calculated from the transconductance, g_m defined as:

$$g_m = (\frac{\partial I_\mathrm{D}}{\partial V_\mathrm{G}})_{V_\mathrm{D}=\mathrm{const}} = \frac{WC_\mathrm{i}}{L}\mu V_\mathrm{D} \qquad (1.2.5)$$

From this equation, it is obvious that μ will be gate-voltage dependent, if the relationship between I_D and V_G is nonlinear. We can also calculate the mobility in the saturation regime by finding the slope of the plot of $|I_\mathrm{D}|^{1/2}$ vs. V_G. (see Eq. 1.2.4) Although it is expected that the linear regime and the saturation regime μ values to be similar for a device, this is not always the case [8]. Source and drain contact resistances or high electric fields often affect the linear regime mobilities. This issue will be investigated in detail in the subsequent chapters.

1.3 Mechanisms of Charge Injection and Transport in Organic Semiconductors

1.3.1 Introduction

The optimal performance of the organic electronic devices, including thin film field-effect transistors and organic light emitting diodes (OLEDs), critically depends on the nature of charge injection from the contacting electrodes into the OSC, followed by the effective transport of the carriers through the bulk of the material. In light emitting diodes [18], the effective injection of the holes and electrons from the contacts is followed by transport through the bulk, leading to recombination and emission of light. In solar cells [18], holes and electrons are generated upon absorption of light, followed by transport through the device and collection at the electrodes, and in FETs, charge injection at the source is followed by transport through the channel and collection at the drain. Since the

underlying principle of operation in all these devices is similar, we will review the different mechanisms of charge injection and transport in the following sections.

1.3.2 Bulk-limited transport

If the contact between the metal and the OSC is Ohmic, with a contact resistance much lower than the resistance of the bulk material (see next section), then the current will be easily injected into the organic material and the transport of charge will be dominated by the bulk [19]. By Ohmic contact we mean the electrode, being an infinite reservoir of charge, can maintain a steady state space-charge limited current (SCL) in the device [4]. In the case where the injected charge dramatically changes the electric field configuration in the polymer (i.e., effectively screens the source-drain field) the transport becomes space-charge limited. In this case, the $I - V$ curves look linear if the field due to the applied bias is the dominant E-field in the device. The conduction is usually linear in the low source-drain bias since the current density in the polymer is low. At higher fields where the current density is very high, there is a significant concentration of charge carriers in transit between the source and the drain. The screening due to these "space charges" produces nonlinear $I - V$ characteristics.

It is important to note that space-charge effects are more readily maintained in materials such as organic semiconductors where the mobility is poor. The low mobility greatly restrains the collection of the carriers at the drain or the recombination of opposite charges. In addition to these effects, OSCs are known to have large concentration of highly localized states (i.e., traps, defects etc) that trap mobile charges temporarily or permanently (immobile charges) [4]. All these factors make organic semiconductors the

perfect breeding ground for space-charge transport.

To obtain a current-voltage relation [20] for samples operating in the space-charge limited currents regime, we can use the current density given by:

$$J = \mu e \rho(x) F(x) \tag{1.3.1}$$

and the poisson's equation:

$$\frac{dF}{dx} \frac{\kappa \varepsilon_0}{e} = \rho(x) \tag{1.3.2}$$

to obtain:

$$J = \mu \kappa \varepsilon_0 F(x) \frac{dF}{dx} \tag{1.3.3}$$

where μ is the mobility defined as the constant of proportionality in the relationship between the applied electric field, F, and the drift velocity of the carriers, ν, given by $\nu = \mu F$, e is the charge of the electron, $\rho(x)$ is the local carrier density, κ is the dielectric constant of the semiconductor material, and ε_0 is the permittivity of the free space. Integrating both sides,

$$Jx = (\mu \kappa \varepsilon_0) \frac{F^2(x) - F^2(0)}{2} \tag{1.3.4}$$

For Ohmic contacts, the electric field at the interface $(x = 0)$ should be zero, that is $F(0) = 0$; so $F(x) = (\frac{2Jx}{\mu \kappa \varepsilon_0})^{1/2}$. Using $V = \int_0^L F(x) \, dx$, we arrive at:

$$J = \frac{9}{8} \mu \kappa \varepsilon_0 \frac{V^2}{L^3} \tag{1.3.5}$$

Eq. 1.3.5 shows that the current rises quadratically with voltage in the space-charge regime. This relationship is called the Child's law, and it holds in materials where the presence of traps and defect states is low. However, realistically, impurities, disloca-tions and rough grain boundaries are commonly observed in many organic materials,

creating shallow or deep trap energy states below the transport energy level [4]. The presence of these unfavorable energy states can influence the transport of charge within the bulk, resulting in non-ideal current-voltage characteristics. Additionally, the effective mobility in many disordered organic semiconducting materials is found to be electric field-dependent [21, 22], (i.e., $\mu = \mu_0 \exp(\gamma \sqrt{F})$, where μ_0 and γ are constants) originating from the intrinsic properties of the material. The effects of this exponentially field-dependent mobility on the $I - V$ characteristics of the OFETs will be discussed at great lengths in Chapter 2.

1.3.3 Hopping nature of transport in organic semiconductors

It was mentioned briefly in the previous section that mobility is defined as the velocity with which charge carriers move under the application of an electric field. In inorganic semiconducting materials, charge transport occurs [4] through wave-like propagation of carriers in well-established conduction or valance bands, with occasional scattering of carriers at impurity sites, lattice dislocations or interactions with phonons. Therefore in these materials, mobilities can reach large values, in excess of 100 cm^2/V.s. However, in OSCs, the constituting molecules are only weakly bound together through van der Waals forces and the traditional view of band formation is not very accurate. In these materials, band energy widths are typically smaller than $k_{\mathrm{B}}T$ [4].

In OSCs, the mobilities are found to be so small ($\leqslant$ 10 cm^2/V.s) that if we were to literally calculate a mean-free path distance for the scattering of the charge carriers, we would obtain values smaller than the intermolecular spacing. In light of this realization, the mechanism of charge conduction in OSCs cannot be the same as that observed in

crystalline materials. In fact, it has to be a rate-limiting process where in each step, charge carriers must overcome an activated energy barrier, with the mobility given by a rate equation [4]:

$$\mu \propto \exp(-E_A/k_B T) \tag{1.3.6}$$

where E_A is the activation energy, and k_B is the Boltzmann constant. In this simple picture, a carrier is initially localized at a particular energy site i, confined approximately within a deep or shallow potential well. Upon receiving enough thermal energy, the carrier can overcome the potential barrier and hop over to a neighboring site, j. This process is illustrated by the cartoon in Fig. 1.7. Thermally assisted *hopping* is the dominant mechanism of transport in organic semiconducting materials. Therefore, the mobility and hence the conductivity of (disordered) OSCs exponentially increase with temperature, which is different from temperature dependence of conductivity in crystalline semiconductors such as Si or Ge. The picture of hopping described above is greatly simplified. In reality the
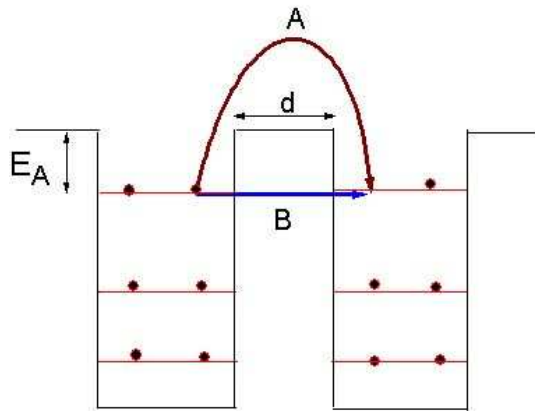
Figure 1.7: Two mechanisms of charge transfer between two localized states: A) Hopping of a charge carrier from one localized state to another upon receiving enough energy to overcome the activation energy barrier E_A, and B) direct tunneling between the 2 states.

density of states and the possibility of both short and long range hops to neighboring sites should be considered. Here we will briefly review a more vigorous mathematical treatment, as described in Ref. [11]:

The two different processes that can take place between two localized states are phonon-assisted hopping or direct tunneling. Tunneling can take place between two localized states if the electronic wavefunctions of the two states effectively overlap, whereas thermally assisted hopping occurs when carriers trapped in localized states absorb a phonon and classically jump to the next available site. The transition rate associated with these two processes is given by:

$$W_{ij} = \nu_0 \exp(-2\gamma R_{ij}) \times \begin{cases} \exp(-(\frac{\varepsilon_i - \varepsilon_j}{k_B T})) & \varepsilon_i > \varepsilon_j \\ 1 & \varepsilon_i < \varepsilon_j \end{cases} \tag{1.3.7}$$

where ν_0 is the attempt frequency, γ is the inverse localization length, R_{ij} is the distance between two localized states and ε_i is energy at site i. The first term on the right side of Eq. 1.3.7 gives the tunneling probability between two states and the second represents the probability of absorbing a phonon for hops upward in energy. Structural disorder and energetics are crucial in hopping transport.

In order to obtain a relationship for the macroscopic conductance in these disordered systems, we use the following approach: In the presence of a weak applied field, the average current flow between two sites can be approximated as a conductance times the difference in the electrochemical potential of the two sites, i. e.,:

$$I_{ij} = G_{ij}(\mu_i - \mu_j) \tag{1.3.8}$$

The steady-state current between any two sites is also given by:

$$I_{ij} = e[W_{ij}f_j(1 - f_i) - W_{ji}f_i(1 - f_j)] \tag{1.3.9}$$

with the occupation probability, f_i as:

$$f_i = \frac{1}{1 + \exp(\frac{(\varepsilon_i - \mu_i)}{k_{\mathrm{B}}T})} \tag{1.3.10}$$

The reason for factors of $(1 - f)$ in Eq. 1.3.9 is to avoid doubly occupied states. Plugging

Eq. 1.3.7 and Eq. 1.3.10 into Eq. 1.3.9, we obtain:

$$I_{ij} = \frac{e\nu_0 \exp\left(-2\gamma R_{ij} - \frac{|\varepsilon_i - \varepsilon_j|}{2k_{\mathrm{B}}T}\right) \sinh\left[\frac{\mu_i - \mu_j}{2k_{\mathrm{B}}T}\right]}{2\cosh\left[\frac{\varepsilon_i - \mu_i}{2k_{\mathrm{B}}T}\right] \cosh\left[\frac{\varepsilon_j - \mu_j}{2k_{\mathrm{B}}T}\right]} \tag{1.3.11}$$

If thermal energy $k_{\mathrm{B}}T$ is small compared to differences in site energies, an approximation

for the conductance between two sites can be obtained from Eqs. 1.3.8 and 1.3.11 and

the definition $\mu_i = \varepsilon_f - e\mathbf{F}.\mathbf{R}_i$ as follows:

$$G_{ij} \approx \frac{e\nu_0}{k_{\mathrm{B}}T} \exp\left(-2\gamma R_{ij} - \frac{|\varepsilon_i - \varepsilon_f| + |\varepsilon_j - \varepsilon_f| + |\varepsilon_i - \varepsilon_j|}{2k_{\mathrm{B}}T}\right) \tag{1.3.12}$$

At this point, several approaches can be taken to obtain the total device conductance,

including constant or energy dependent density of states around the Fermi energy or by

using the methods of percolation theory [23]. Here we will show the simplest approach

undertaken originally by Mott. This is the essence of variable range hopping (VRH).

In Mott's picture, with a constant density of states, a carrier that is close to the Fermi

energy can hop a distance R and to as many as $\frac{4}{3}\pi R^3 \rho \Delta \varepsilon$ sites. By putting a constraint

of one hopping site on the carrier, $\frac{4}{3}\pi R^3 \rho \Delta \varepsilon \sim 1$ and substituting this into 1.3.12 and

noting that $|\varepsilon_i - \varepsilon_f| + |\varepsilon_j - \varepsilon_f| + |\varepsilon_i - \varepsilon_j| = 2|\varepsilon_i - \varepsilon_f| = 2\Delta \varepsilon$ for $\varepsilon_i > \varepsilon_j$, we obtain:

$$G \propto \exp\left[-2\gamma R - \frac{1}{k_{\mathrm{B}}T(4/3)\pi R^3 \rho}\right] \tag{1.3.13}$$

The optimum conductance is when G is maximized with respect to R. Doing so, we

obtain the famous Mott's law:

$$G \propto \exp\left[-\left(\frac{T_0}{T}\right)^{1/4}\right] \quad \text{where} \quad k_{\mathrm{B}}T_0 \sim \frac{\gamma^3}{\rho} \tag{1.3.14}$$

Notice that the conductance decreases with decreasing T, as it is a characteristic of hopping conduction in disordered semiconductors. The treatment above is oversimplified since it ignores electron-electron interactions, or an energy dependent density of states. There are several more sophisticated treatments of the hopping conductivity in disordered organic semiconductors. In reality, most models have serious limitations and cover only certain transport ranges with reasonable validity.

1.3.4 Injection-limited transport

In addition to the intrinsic (bulk) properties of the semiconducting polymers in transporting the electronic charge, the interface between the OSC and the contacting electrode (usually a metal such as Au, Pt or Al) also plays an important role in the overall operation of the organic electronic devices. If the bottleneck in charge transport is injection at the contacts, a device is said to be injection or contact limited. In this case, the metal/OSC interface may show Ohmic or nonlinear $I-V$ characteristics. The band offset between the metal work function and the HOMO or LUMO level in the OSC (depending on whether the transport is p- or n-type) is one important factor in determining the type of contact at the interface [3, 24]. If there is a sizable potential energy barrier from the metal into the transporting band in the OSC, the charge injection would be poor and the contact resistance will dominate the device operation. However, many factors such as electrode work function, doping levels, interfacial traps or dipoles etc. influence the band alignment at the interface. One objective of this thesis is to investigate each of these factors in detail and therefore we will leave their discussion until the appropriate chapter. In what follows below, we will outline the approaches taken so far to explain the experimental charge

injection results at OSC/metal interfaces and we point to the strengths and deficiencies of these models.
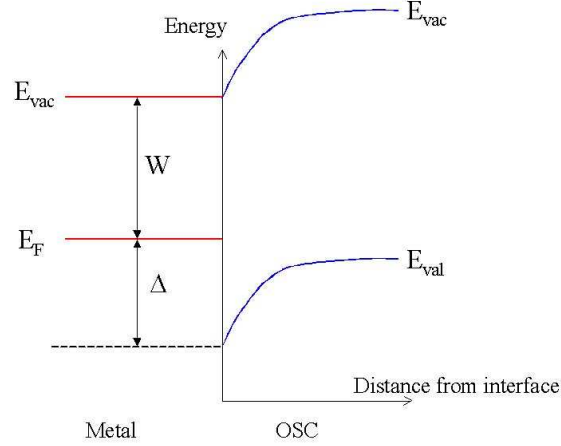
Figure 1.8: The thermionic emission model: Upon acquiring enough thermal energy, a carrier (in this case a hole) overcomes the intrinsic potential barrier, $\Delta = W - I_{\mathrm{p}}$, at the interface and is injected into the valance band of the OSC.

One theoretical approach used commonly to explain the charge injection results in organic semiconducting devices is the thermionic emission model: Upon acquiring enough thermal energy, a carrier overcomes the intrinsic potential barrier, $\Delta = W - I_{\mathrm{p}}$, at the interface and is injected into the polymer. Here, W is the metal work function and I_{p} is the ionization potential of the OSC [18]. The energy band diagram for (hole) charge injection of this nature is illustrated in Fig. 1.8. In one (more realistic) version of this theory [24], the effect of Δ is modified by contributions from the external electric field potential and the image charge potential as follows:

$$ J = \frac{em^*}{2\pi^2\hbar^3}(k_{\mathrm{B}}T)^2 \exp\left(\frac{-e\Delta}{k_{\mathrm{B}}T}\right) \exp(f)^{1/2} \left[\exp\left(\frac{eV}{k_{\mathrm{B}}T}\right) - 1\right] \tag{1.3.15} $$

where m^* is the effective mass and $\hbar$ is the reduced Planck's constant. The second

exponential term accounts for the lowering of the barrier height due to the electric field at the interface, where $f = e^3 F/4\pi\epsilon_0\epsilon k_{\mathrm{B}}^2 T^2$. The last exponential factor corrects for the effect of the applied voltage and the -1 term ensures that no current should flow when there is no applied voltage. Although this equation has been used rather frequently to fit the data in OSC/metal contacts (usually at high T and low F), it's not entirely relevant because it ignores the fact that OSC have intrinsically low mobilities and surface recombination is expected [19]. Additionally, the localization of charge carriers upon injection into the polymer is unaccounted.

In a separate work, Emtage and O'Dwyer [25] considered the drift-diffusion of charge carriers in the space-charge regime at the vicinity of the contacts. In the limit where the polymer is diffusion-controlled and scattering of charge carriers is an issue, the diffusion-limited thermionic emission current is given in the low-field limit by:

$$J = Ne\mu F \exp(-e\Delta/k_{\mathrm{B}}T) \tag{1.3.16}$$

and in the high fields:

$$J = N\mu \left(\frac{k_{\mathrm{B}}T}{e}\right)^{1/2} (16\pi\epsilon_0\epsilon e F^3)^{1/4} \exp\left(\frac{-e\Delta}{k_{\mathrm{B}}T}\right) \exp(f)^{1/2} \tag{1.3.17}$$

N here is the carrier density. In this model, the motion of carriers is considered in a potential given by: $\varphi = \Delta - F_0 x - e/4\epsilon_0\epsilon$, where F_0 is the electric field strength at the immediate vicinity of the contact. The last term on the right hand side is due to image charge attraction. Notice that the temperature dependence of the current is still given by the intrinsic energy barrier height, Δ, minus the barrier lowering effect at high fields.

Thermionic emission is usually more significant at high temperatures where the carriers have sufficient thermal energy to overcome the potential barrier. At very low temperatures, or in the cases where the height of the potential barrier is relatively large, thermionic emission loses its significance. In such situations, carriers are injected only by means of quantum mechanical tunneling through the barrier. This process is called field emission and is the dominant injection-limited mechanism at high fields and low temperatures. The $J - V$ is predicted by the Fowler-Nordheim equation given below [18]:

$$J = \left(\frac{e^3}{8\pi h \Delta} \right) F^2 \exp \left(-\frac{8\pi \sqrt{2m^* \Delta^{3/2}}}{3heF} \right) \tag{1.3.18}$$

This treatment, which is purely quantum mechanical, also ignores the presence of localized states at the OSC side of the interface. Additionally, in all the discussion above the disordered nature of the semiconductor was ignored. In more recent sophisticated models [26], hopping injection from the metallic electrode into an energy-dependent (Gaussian) density of localized states in the valance band is followed by diffusion into the polymer bulk. In such models, carriers can hop into lower energy states in the tail of the distribution, therefore enhancing the charge injection, specially at lower temperatures. This affects the temperature dependence of the injected current and will be examined in detail in Chapter 3.

1.4   This Thesis

This thesis is primarily focused on the topic of charge transport and injection in organic field-effect devices. Our main objective is to understand the physical principles governing the motion of charge carriers in these devices. This means that rather than concentrating on optimizing device performance by using various organic semiconductors or

sample preparation techniques, we have chosen one well-established OSC, namely P3HT, and performed experiments that seemed crucial in understanding the physics of device transport. The results and analysis of the data follow in the next four chapters. Each chapter is broken into several sections and subsections, typically with the main headings of Introduction, Experimental Details, Results and Analysis and Conclusions.

In Chapter 2, we investigate the issue of nonlinear charge transport in very short channel devices over a broad range of temperatures and gate voltages. The nonlinearity observed in the current-voltage characteristics of the devices, specially at low temperatures and high gate voltages is attributed to a model of space charge limited transport with an exponential dependence of mobility on the applied electric field. We considered the possibility of contact effects in this set of devices and showed that the data is more indicative of bulk-limited transport.

In Chapter 3, we turn to investigate the physics of contacts in our organic transistors. We fabricated several devices with various metallic contacts to the OSC and thoroughly measured the transport characteristics as a function of temperature. This chapter is divided into two main sections of Linear vs. Nonlinear charge injection. Linear transport, which is observed in devices with high contact metal work function, is analyzed in the context of a modified diffusion-limited thermionic emission model. An inverse relationship between the channel mobility and the contact resistivity is observed over 4 decades of mobility and is in good agreement with this model. Nonlinear charge injection from low metal work functions, however, shows a weak temperature dependence that is in contradiction with thermionic models. We find that a model of charge injection from metallic electrodes into a disordered density of states in the OSC, with emphasis on the

primary injection event, accounts well for the field and temperature dependence of our devices. This is consistent with previous experiments in OLEDs.

In Chapter 4, we consider charge injection into P3HT as a function of impurity dopants present in the OSC. As devices are annealed in vacuum and at elevated temperatures, the concentration of these dopants, believed to be mainly oxygen and water, is significantly reduced, affecting the nature of charge injection. From high to low doping, the transport in Au devices changes from linear to nonlinear, indicating a possible change in band alignment at the metal/organic interface. In a collaboration with a group at University of Rochester, ultraviolet photoemission spectroscopy was performed on several samples to see the effect of annealing on band alignment. The results were consistent with the transport measurements, indicating the formation of an increased barrier for carrier injection.

Finally in Chapter 5, we discuss the results of a short study on charge injection into P3HT transistors, with source and drain electrodes modified by self-assembled monolayers prior to polymer deposition. This work was performed in collaboration with Prof. James Tour's group in the Chemistry Department. These molecules were used to shift the effective work function of Au electrodes, therefore markedly affecting the charge injection process. The contact resistance vs. mobility data for the molecules increasing the metal work function is systematically examined and an explanation is provided.

Chapter 2

AN INVESTIGATION OF NONLINEAR CHARGE TRANSPORT IN ORGANIC FIELD-EFFECT TRANSISTORS

2.1 Introduction

As we discussed in the previous chapter, field-effect mobility in OFETs is an important parameter in describing charge motion within the conducting channel. In disordered polymer semiconductors this mobility, μ, is strongly temperature dependent near room temperature, consistent with thermally assisted hopping between localized states dispersed throughout the polymer film [27]. These localized states are likely to be polaronic [28]. Several different models for hopping transport in these materials have been used to interpret experimental data from $\sim$200 K to room temperature, including simple thermal activation [29], 2d variable range hopping (VRH) [30], and percolative VRH with an exponential density of states [23]. While some models work better with some specific samples, generally distinguishing between them is difficult as we will show in section 2.3.

The situation is complicated by the fact that the effective mobilities inferred in this manner depend on T, gated charge density [31], source-drain bias, and contact effects. Parasitic contact resistances in particular can be important. Experiments in several OSC/electrode combinations [32, 33, 14], [34, 35, 36, 37, 38] have shown that contact resistances can be a significant fraction of the total source-drain resistance in the linear regime in short-channel devices. Data in this shallow channel limit must be corrected

accordingly for this parasitic series resistance, R_s, to find the true mobility within the semiconductor. We will come back to this issue at great lengths in the following chapter. As with μ, one must bear in mind that R_s typically depends on temperature, gate voltage, and local electric field [34]. When examining transport properties of organic FETs, it is imperative to determine whether the devices are dominated by the bulk (channel) or the contacts.

This chapter investigates *nonlinear* transport measurements in field-effect devices made from high quality, solution cast, regioregular poly(3-hexylthiophene) (P3HT), with channel lengths from 3 μm to 200 nm and aspect ratios (W/L) of 10. Higher temperature properties at low source-drain fields are consistent with those observed by other investigators. From 200 K to 10 K, we observe gate-modulated nonlinear IV characteristics. To understand the effects of contacts in our series of devices, we examined both the devices described above, and an additional series of fixed-width FETs to obtain the channel and contact resistances as a function of temperature. These data demonstrate that (a) the fixed-aspect-ratio devices are bulk (not contact) limited at high temperatures; and (b) the contribution of contacts relative to the channel actually *decreases* as the temperature is lowered, so that bulk-limited devices tend to remain so as T is decreased. Since the nonlinearities in the IV curves become more pronounced at low temperatures and in wider devices (for which contact resistance are proportionately less important), it is unlikely that these nonlinearities are due to contact effects in these geometries. We find that the nonlinear data are consistent with a model of Poole-Frenkel (PF) type conduction in the space-charge limited (SCL) regime. Within this framework, the strong gate and temperature dependence of this conduction are consistent with a density of localized

valence states that varies approximately exponentially in energy. Still within this model, at temperatures below 30 K there appears to be a crossover from thermally assisted hopping to a non-thermal mechanism. These nonlinear data over a broad temperature range constrain any other models of transport in such devices. Studying FETs in this nonlinear regime allows comparisons between models not readily performed with linear transport data.

2.2 Experimental Details

Devices are made in a bottom-contact configuration (see Fig. 1.4(left) in Chapter 1.) on a degenerately doped $p+$ silicon wafer to be used as a gate. The gate dielectric is 200 nm of thermal SiO_2. Source and drain electrodes are patterned using standard electron beam lithography. The electrodes are deposited by electron beam evaporation of 4 nm Ti and 25 nm of Au followed by liftoff. The fixed-aspect-ratio devices have channel lengths ranging from 3 μm down to 200 nm, with the channel width scaled to maintain $W/L = 10$. Fig. 2.1 shows an example of one of these narrow gap electrodes. Larger FET devices ($W = 1$ mm, $L = 50$ μm) are also prepared by evaporation through a shadow mask for comparison. We also examine a second set of devices with fixed width $W = 100$ μm and channel lengths varying from 5 μm up to 40 μm, specifically for probing contact resistance issues.

The organic semiconductor is 98% regioregular P3HT [39], a well studied material [40, 41, 42]. P3HT is known from x-ray scattering to form nanocrystalline domains with sizes on the order of 20 nm [40, 41, 42], and more ordered films correlate with higher measured mobilities. RR-P3HT is dissolved in chloroform at a 0.02% weight
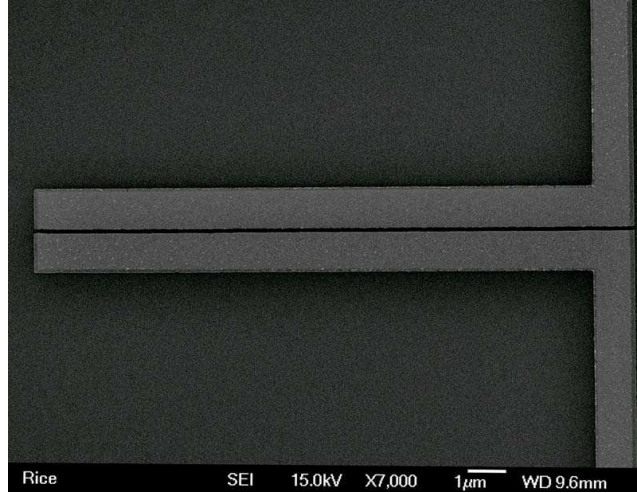
Figure 2.1: A pair of lithographically designed Au electrodes with a separation gap of ~ 100 nm. P3HT is deposited directly on top of this pattern, filling the gap between the 2 electrodes.

concentration, and is solution cast [40] onto ozone-cleaned, chloroform-swabbed substrates. The fixed-aspect-ratio series of devices are from one casting, while the fixed-width series are from a second casting. The resulting film thicknesses over the channel region are tens of nm as determined by atomic force microscopy (AFM). All devices are stored in vacuum desiccators until use. The measurements are performed in vacuum ($\sim 10^{-6}$ Torr) in a variable-temperature probe station using a semiconductor parameter analyzer (HP4145B).

2.3   Results and Discussions

At room temperature, the devices operate as standard p-type FETs in accumulation mode [30, 40, 41, 42, 43]. With the source electrode as ground, in the linear regime we extract [29] an effective mobility from the transconductance (see section 1.2.3 for details). That is, from data of source-drain current, I_D versus the gate voltage, V_G, at

a fixed low drain voltage, V_D, we compute $\mu = (g_m L)/(W C_i V_D)$, where $g_m \equiv \partial I_D / \partial V_G$ is the transconductance, C_i is capacitance per unit area of the gate insulator, and L/W is the aspect ratio. In cases where the parasitic resistance of the source and drain is high, the relationship for linear-regime mobility has to be modified. We will return to this in Chapter 3. As is reported elsewhere [32], the mobility is gate-voltage dependent, increasing with increasing V_G. It also increases with increasing source-drain voltage. Effective mobilities are typically between 10^{-3} and 10^{-2} cm^2/Vs, and apparent threshold voltages (V_T), though not necessarily meaningful [43], are low (< 2 V) (In MOSFETs, V_T corresponds to the onset of inversion [12] while OFETs strictly work in accumulation mode). For $L = 50$ μm FETs operated in the saturation regime, the on/off ratio is typically $\sim$ 650, comparing between gate voltages of -95 V and 0 V. As temperature is reduced below 300 K, the off-current drops to undetectable levels by 150 K, as the unintentional carriers (due to slight doping from air exposure) freeze out.

From room temperature (300 K) to $\sim$ 200 K, the mobility as inferred above at fixed small V_D is found to depend steeply on temperature. A small representative set of this data is shown in Fig. 2.2, where μ is plotted vs. inverse temperature for $V_G = -30, -40,$ and -50 V, for the $L = 300$ nm, $W = 3$ μm device at constant source-drain electric field of 1.3×10^7 V/m.

These data are approximately equally consistent with the three models mentioned above: simple Arrhenius behavior (the dashed line) with an activation energy ~ 100 meV; VRH for a 2-d system (dotted line), of the form $\mu = \mu_0 \exp(-(T_0/T)^{1/3})$, where μ_0 and T_0 are fit parameters; and finally the more sophisticated percolative VRH theory (solid lines) developed by Vissenberg et al [23, 43]. The Vissenberg model's underlying assumptions
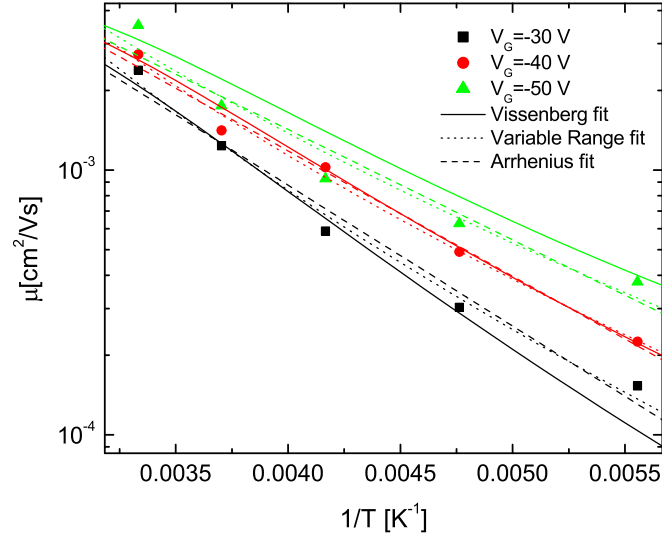
Figure 2.2: Mobility vs. T as computed from transconductance for three gate voltages, for a device with $L = 300$ nm from room temperature down to 200 K. Lines are fits to various models of hopping transport described in the text.

include an exponential density of (localized) states (DOLS), $\nu(\epsilon) \sim \exp(\epsilon/k_\mathrm{B}T_0)$, with transport of carriers dictated by percolative hopping. Since the gate voltage controls the Fermi level in the channel, and hence the occupation of the localized states, one finds that transport in the channel is strongly affected by V_G. Relevant fit parameters [23, 43] are: T_0, describing the energy dependence of the DOLS; a prefactor σ_0 with units of conductivity; and α, an effective overlap parameter for tunneling between two hopping sites. Values used in the fits shown are $\sigma_0 = 7 \times 10^5$ S, $T_0 = 418$ K, $\alpha = 4.35 \times 10^9$ m^{-1}, consistent with those seen by other investigators in P3HT [43].

As temperatures are lowered from 200 K down to 10 K, over a broad range of source-drain and gate voltages, I_D evolves from approximately linear to a strongly nonlinear

(superquadratic) dependence on V_D. An example of this evolution is shown in Fig. 2.3 for the $L = 3$ μm, $W = 30$ μm device, comparing data at 300 K and 70 K. We note that, at the lowest temperatures, smaller devices transport current *more easily* (larger currents at smaller gate voltages for a fixed V_D/L) than larger devices, as we will discuss later.
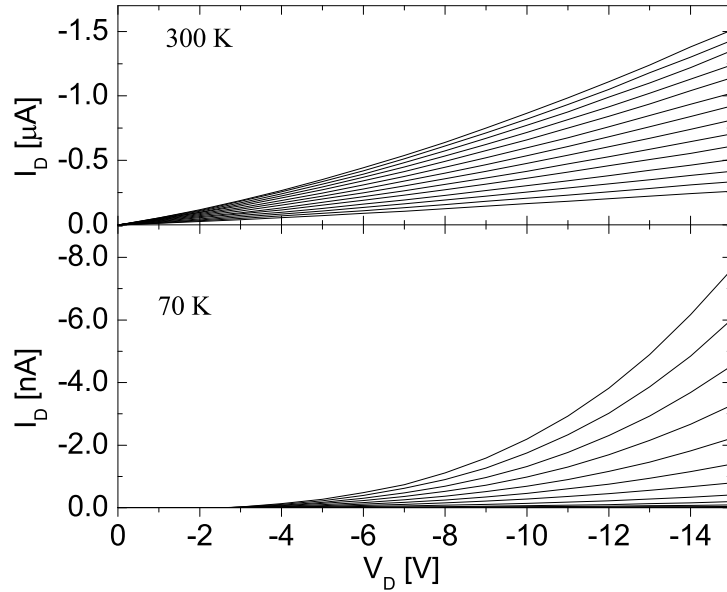
Figure 2.3: I_D vs. V_D for the $L = 3$ μm, $W = 30$ μm device, at 300 K (nearly linear, top) and 70 K (highly nonlinear, bottom). Curves from the top down correspond to V_G values from -95 V to -30 V in intervals of 5 V.

Analysis below shows that the nonlinear IV characteristics are described well by a model incorporating space-charge limited currents, modified by a Poole-Frenkel-like exponential dependence of effective mobility on square root of the local electric field (SCLPF). This conduction mechanism has been seen repeatedly in *two*-terminal devices [22, 44]. Room temperature experiments [45] on P3HT FETs with 70 nm channel lengths also show indications of SCL currents. We find that within this model, the temperature and

gate voltage dependence of the data support a strongly energy dependent DOLS such as that in the Vissenberg picture. Other models may be possible, but they are constrained by the dependencies presented below.

As described in section 1.3.2, charge transport in a device is space-charge limited if the injected carriers significantly alter the local electric field from the average field imposed by the electrode potentials, and correspondingly limit the current. If, instead, the bottleneck in charge transport is injection at the contacts, a device is said to be contact limited, and is expected to exhibit Ohmic behavior at low source-drain fields. In principle, modeling our devices requires the full solution of the steady state charge and electric field profile in a three-terminal accumulation mode transistor, including field- and temperature dependent effective mobility, and field- and temperature dependent contact properties. This general problem is very complex [46]; here we consider a simpler model and compare with the transport data.

In a system that is not contact limited, when the effective mobility varies as a function of electric field F, the space-charge limited current in a two-terminal device (a 1d model) is determined by the numerical solution of Eq. 1.3.3. We note that the case of an effective mobility that varies as

$$\mu(F) = \mu_0 \exp(\gamma \sqrt{F}) \tag{2.3.1}$$

and Ohmic contacts has been solved [20], and that the exact numerical solution is very well approximated by:

$$I \approx \frac{9}{8} \kappa \epsilon_0 \mu_0 \left(\frac{V}{L}\right)^2 \frac{A}{L} \exp\left[0.9\gamma \left(\frac{V}{L}\right)^{1/2}\right]. \tag{2.3.2}$$

Here A is the device cross-sectional area, and L is the interelectrode distance. In our

geometry L is the channel length, A is an effective cross-sectional area for the device (proportional to channel width), and κ is the relative dielectic constant of the semiconductor (chosen to be 3 in our analysis). The appearance of V/L in this equation does not imply that the electric field is constant over the device length. Rather, Eq. 2.3.2 suggests a means of plotting IV data to quickly ascertain consistency with the detailed numerical solution to the two-terminal SCLPF problem.

Note that μ_0 can depend on temperature; in a picture of hopping it should be proportional to the effective DOLS at the injecting contact. The dependence of mobility on $\exp(\sqrt{F})$ has long been seen in semiconducting and conducting polymers [21], and is associated with the charge carriers and disorder in these materials [28, 22, 47, 48]. The numerical solution of Ref. [20] (approximated by Eq. 2.3.2) should be valid as long as the functional form of the field-dependent mobility remains $\exp(\sqrt{F})$.

This equation is derived [20, 44] assuming that the charge distribution is determined by source-drain electrostatics only. The electric field from the gate certainly plays a nontrivial role in our devices, clearly affecting charge injection, and allowing the formation of a channel at higher temperatures (since any charge present in the channel below dopant freeze-out has to be injected from the source and drain). For simplicity, however, in this model we will assume that the gate dependence will manifest itself through μ_0, and that for fixed gate voltage we may treat the source-drain conductance like a two-terminal device.

Figure 2.4 a shows a representative log-log plot of I_{D} vs. V_{D} for one sample with $L = 500$ nm and $V_{\mathrm{G}} = -75$ V, for several temperatures. The solid lines are the numerical solution to Eq. 1.3.3, with parameters $A\mu_0$ and γ chosen at each temperature to give the
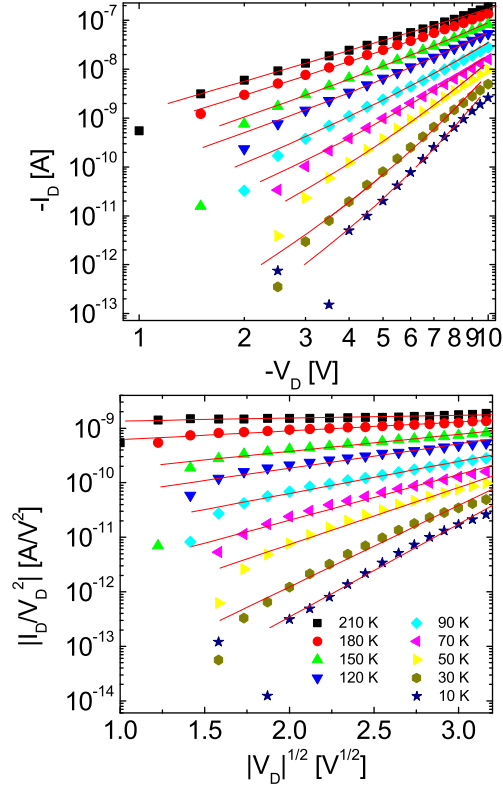
Figure 2.4: (a) Log-Log plot of I_D vs. V_D for a device with $L = 500$ nm at $V_G = $ -75 V. Solid lines indicate a numerical solution assuming space-charge limited conduction with a Poole-Frenkel-like field dependence of the mobility. (b) Plot of $\ln(I_D/V_D^2)$ vs. $\sqrt{V_D}$, as suggested by Eq. 2.3.2. Solid lines are fits to a linear dependence on $\sqrt{V_D}$.

best fit. The numerical solution is virtually indistinguishable from the analytic form of Eq. 2.3.2. Data on this and other samples for different gate voltages are qualitatively similar, with very good agreement between the numerical solution of the SCLPF model and the data. Fig. 2.4 b shows the same data and fits replotted as suggested by Eq. 2.3.2. The quality of this agreement between the SCLPF model and the data in several devices over a broad range of T, V_G, and V_D/L is striking. Clearly for a given (large) V_G and (low) T, $I_D \sim V_D^2 \exp(\sqrt{V_D})$. Alternate explanations of the nonlinear conduction are

strongly constrained by this dependence. The temperature and gate voltage range over which this form of source-drain nonlinearity occurs varies systematically with sample size, as described below.

2.3.1 Contact effects

One must consider whether the nonlinear $I_D - V_D$ characteristics result from nonlinear contact resistances (presence of a Schottky barrier at the metal/OSC interface) as the temperature is decreased. For several reasons, discussed below, we do not believe this to be the case.

First we consider directly inferring the contact and channel resistances (R_s and R_{ch}, respectively) in the linear regime, and examining the temperature variation of their relative contributions. For a series of devices with fixed width, these resistances are calculated as follows [35, 36, 37, 38]: At a given T, the total resistance, $R_{on} \equiv \partial I_D/\partial V_D$, is calculated for each device at a small V_D and is plotted as a function of L for each gate voltage. The channel resistance per unit length, R_{ch}/L, at a given T and V_G is the slope ($\partial R_{on}/\partial L$) of such a graph, and the intercept (R_{on} extrapolated to $L = 0$) gives the parasitic series resistance, R_s.

For a fixed-aspect-ratio series of devices, one may follow an analogous procedure. The total source-drain resistance $R_{on} = (L/W)R_\square + R_s$, where $R_\square$ is the resistance per square of the channel. At a given T and V_G, $R_{on} \times W$ is plotted versus L for the series of devices. The slope of such a graph gives $R_\square$, and the intercept gives the total parasitic contact resistivity, $R_s \times W$. This analysis is shown in the fixed-aspect-ratio devices in Fig. 2.5 at room temperature for several gate voltages. For our geometry of $W/L = 10$, the inset
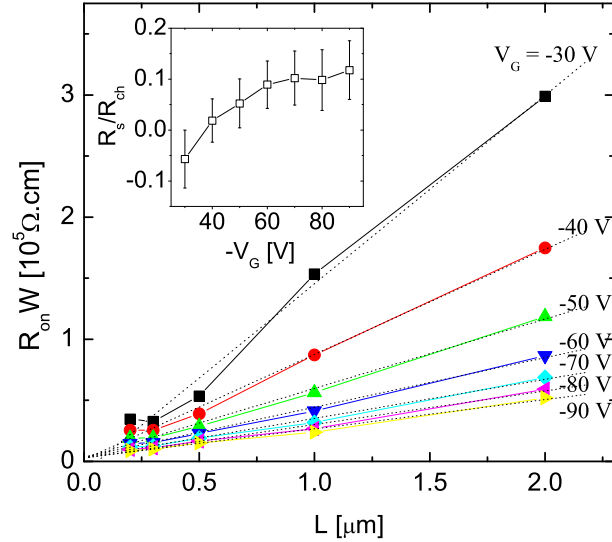
Figure 2.5: Plot of $R_{\mathrm{on}} \times W$ vs. L for the fixed-aspect-ratio device series in the linear regime at 300 K for several gate voltages. Slopes of the linear fits correspond to $R_{\square}$ of the channel, while intercepts correspond to the parasitic contact resistivity, $R_{\mathrm{s}}W$. Inset: the ratio $R_{\mathrm{s}}/R_{\mathrm{ch}}$ for the $L = 1$ μm, $W = 10$ μm device. Clearly this device is *not* contact limited at room temperature. At low gate voltages, the intercepts from the fits give negative values for R_{s}. However, the error bars are significant and although the devices may have small positive contact resistances, these values are negligible compared to the channel resistances.

shows the inferred $R_{\mathrm{s}}/R_{\mathrm{ch}}$ as a function of V_{G}, for a device with $L = 1$ μm. Our series of fixed-aspect-ratio devices is clearly channel-limited at room temperature.

This analysis may be repeated at different temperatures to examine the evolution of R_{s} and R_{ch}. We find that the nonlinear conduction at large average source-drain fields shown in the previous section makes this difficult to measure over a broad temperature range in the fixed-aspect-ratio device series. However, the fixed-width devices with longer channel lengths are well-suited to this approach down to 100 K. Figure 2.6 shows $R_{\mathrm{s}}/R_{\mathrm{ch}}$ as a function of temperature for the $L = 5$ μm device from the $W = 100$ μm series. Near
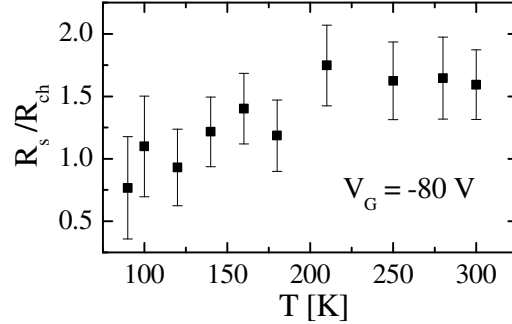
Figure 2.6: $R_{\rm s}/R_{\rm ch}$ as a function of temperature as determined for the $W = 100$ μm, $L = 5$ μm member of the fixed-width set of devices. Since this ratio decreases as T is lowered, contacts actually *improve* relative to the channel at low temperatures. This interesting result will be discussed more fully in the next chapter.

room temperature, $R_{\rm s} > R_{\rm ch}$ for this device. As T decreases, while both $R_{\rm s}$ and $R_{\rm ch}$ increase significantly, $R_{\rm s}$ falls below $R_{\rm ch}$ near 100 K. The results of this experiment and others, which will be presented in more detail in the next chapter, demonstrate that the contact contributions become *less* important at low temperatures. This strongly suggests that the nonlinearities in the $I_{\rm D} - V_{\rm D}$ curves of short channel length devices observed at lower temperatures are unlikely to be contact effects.

Furthermore, the trends in transport with sample dimensions also support this conclusion. We find at low temperatures that the smallest devices actually transport charge considerably *better* than larger devices. For example, at 50 K for fixed $V_{\rm D}/L$, the fixed-aspect-ratio $L = 300$ nm device exhibits measurable conduction for gate voltages as small as -25 V, while the $L = 3$ μm device requires $V_{\rm G} = -45$ V. This trend is the *opposite* of what one would expect for contact-limited conduction [14]. Since W/L is held constant in this set of devices, shorter devices have significantly smaller contact areas as well, further emphasizing this point. The data are, however, consistent with the suggestion of

space charge effects seen in 70 nm channel length P3HT FETs [45]. Finally, the voltage and temperature dependence of the data in Fig. 2.4 is not consistent with the forms for either classical Schottky contacts (Eq. 1.3.15) or Fowler-Nordheim (Eq. 1.3.18) emission. Detailed theory [26] and experiments [49] on injection into disordered polymer semiconductors show that injection efficiency can actually *improve* as temperature is decreased, consistent with our contact resistance data described above. Coupled with the size dependence, this supports the idea that low temperature transport in our devices is *bulk* limited rather than contact limited.

2.3.2   Physical significance of fit parameters

Continuing within the SCLPF model and our analysis of the fixed-aspect-ratio devices, we note that, for identical effective mobilities and γ parameters, Eq. 2.3.2 implies that two samples with the same aspect ratio, thickness, and average source-drain field should give the same currents, independent of channel length, even deep in the nonlinear regime. Device-to-device variability in the effective mobility and γ, presumably due to differences in P3HT thickness and microstructure, make this challenging to check directly in our devices. For reasonable values of γ and V_{D}/L, a 10% variation in γ would lead to more than a factor of two variation in predicted current at low temperatures because of the exponential dependence in Eq. 2.3.2. However, if one fixes V_{D}/L and V_G, and normalizes measured currents by room temperature mobilities, one does indeed find scaling. For example, the $L = 500$ nm and $L = 1$ μm currents in the nonlinear regime normalized this way agree well all the way down to 10 K.

Within this model, the parameter γ should depend only on the hopping mechanism
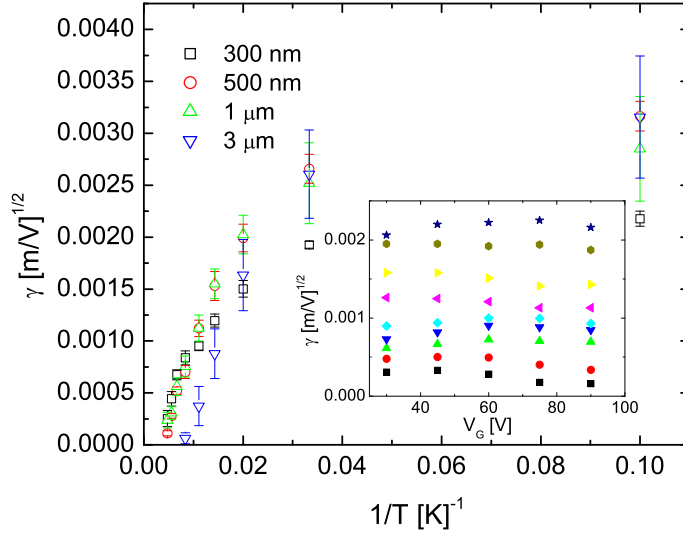
Figure 2.7: Inset: Plot of the parameter γ vs. V_{G} for the 500 nm sample of Fig. 2.4 at various temperatures ((top-to-bottom) 10 K, 30 K, 50 K, 70 K, 90 K, 120 K, 150 K, 180 K, 210 K) showing that γ is roughly gate voltage independent. Main figure: Plot of γ vs. $1/T$ for several samples, with γ averaged over gate voltages for each sample. Error bars are standard deviation. At high temperatures γ is expected to vary linearly in $1/T$, and all samples show a similar slope, $\gamma \times T \approx 0.12$ $(\mathrm{m/V})^{1/2}$. Within this model, saturation of γ at low temperatures would indicate a crossover from thermal to nonthermal hopping transport at low temperatures.

(*e.g.* thermal activation) and the nature of the localized states. We therefore expect γ to be independent of gate voltage for a given sample, and this is indeed seen in the inset to Fig. 2.7. At high temperatures ($T > 50$ K), the data for all gate voltages and all samples look roughly linear in $1/T$, consistent with thermally activated hopping. The magnitude of the slope of γ vs. $1/T$ is approximately 0.12 $\mathrm{K(m/V)}^{1/2}$. This is consistent in magnitude with coefficients found in other semiconducting polymers such as poly(phenylene vinylene) [22]. However, γ vs. $1/T$ deviates significantly from a straight line at lower temperatures for all samples. This is consistent with a crossover from

thermally activated hopping to a much less steep temperature dependence. A natural candidate is field enhanced tunneling between the localized states.
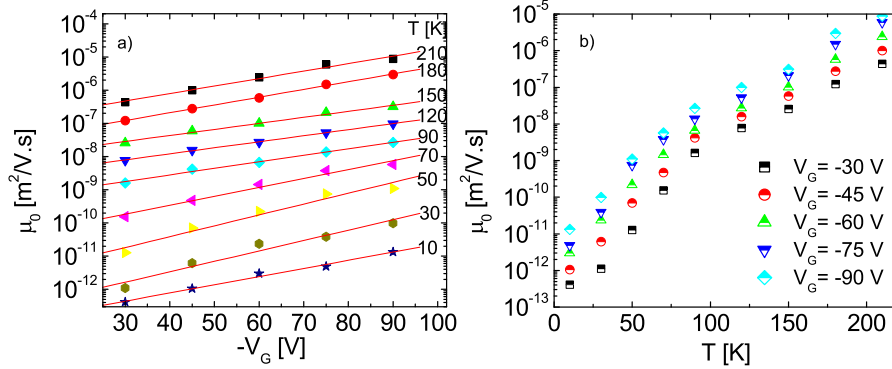
Figure 2.8: Assuming a fixed effective area $A = 3 \times 10^{-13}$ m^2, (a) Plot of the parameter μ_0 from plots like Fig. 2.4 vs. V_G for the 300 nm sample, from 210 K down to 10 K. (b) Plot of μ_0 vs. T for the same sample, for 5 different gate voltages. Note that μ_0 depends nearly exponentially on both temperature and gate voltage.

We now consider the gate and temperature dependence of the parameter $A\mu_0$ found by the numerical analysis above. The effective cross-section for current flow, A, is assumed to be temperature and gate voltage independent for each sample. In the linear regime at moderate temperatures, it is known that the mobility inferred from the transconductance is gate voltage dependent, as seen in Fig. 2.2. This dependence on V_G continues in the apparent SCLPF regime, as shown in Fig. 2.8a on an $L = 300$ nm device. The amount of variation of μ_0 with V_G, roughly a 5% increase of μ_0 per volt of V_G for this sample, shows no strong trend with temperature. The magnitude of this variation of mobility with V_G is consistent with that seen at higher temperatures in Fig. 2.2 for this sample. This exponential dependence of μ_0 on V_G is seen throughout the apparent SCLPF regime. As

in the linear regime of an accumulation FET, gate voltage modulation of the conduction is *unipolar*: higher currents result only when V_G is made more negative.

The temperature dependence of μ_0 is also very strong, as shown in Fig. 2.8b for the same 300 nm channel sample at five gate voltages. The variation of $\mu_0(T)$ shown is much closer to an exponential in T to some slightly sublinear power rather than an Arrhenius or VRH form. This strong temperature dependence of μ_0 holds for all samples in the apparent SCLPF regime.

The strongly energy dependent DOLS employed in, for example, the Vissenberg model offers a natural explanation for these steep dependencies of μ_0 on V_G and T. In the absence of any gate effect, the effective density of localized states available for hopping transport at some temperature T is given by $\nu(\epsilon \approx k_B T)$ where energy is measured from the band edge. An exponential DOLS of the Vissenberg model would then lead to an exponential dependence of μ_0 on T. Gate voltage dependence in this case comes from electrostatic modulation of the Fermi level in this rapidly varying DOLS. It is difficult to understand otherwise how an exponential dependence of the prefactor on T or V_G could arise. Deriving a quantitative relationship between V_G and the local Fermi level would require solving the full electrostatic problem of SCPLF conduction in the presence of the transverse gate field.

One can consider whether the proposed SCLPF conduction is a *bulk* process or one dominated by conduction in the thin channel layer active in standard FET operation. For the SCLPF mobility parameter μ_0 to coincide with the zero field mobility found at high temperatures in the linear regime, an effective cross-sectional area A considerably larger than $W \times$ a few nanometers is required. This is also true for the data of Ref. [45],

in which a considerably different device geometry was used, if analyzed using the SCLPF model. However, the model of Eqs. 1.3.3 and 2.3.1 does not account for the presence of a gate electrode or complicated source and drain geometries, and full computational modeling in this regime may be required to quantitatively account for this. One test for bulk vs. channel conduction would be to search for a correlation between P3HT thickness and currents in the apparent SCL regime.

2.4   Conclusions

For a series of field-effect devices with channel lengths ranging from 3 μm to 200 nm, we find gate modulated nonlinear conduction at low temperatures and high average source-drain electric fields. Analysis of channel and contact resistances as a function of temperature, and the dependence of conduction on sample size at low temperatures support the conclusion that this nonlinearity is unlikely to be a contact effect. We find that the data are well described by a model of gate modulated space-charge limited currents with Poole-Frenkel-like behavior of mobility. Within this model, the V_G and T dependence of the mobility prefactor is consistent with a very strongly energy dependent density of localized states. Finally, the temperature dependence of the Poole-Frenkel-like term within this model suggests a crossover from thermal hopping to quantum tunneling at low temperatures. Further studies of the field effect electrostatics problem, the OSC/metal contacts, and the low temperature non-thermal hopping process should lead to increased understanding of the conduction processes at work in these materials.

Chapter 3

CHARGE INJECTION INTO ORGANIC FIELD-EFFECT TRANSISTORS FROM VARIOUS METALLIC ELECTRODES

3.1 Introduction

In this chapter, we investigate at length the issue of contact resistances between the OSC (P3HT) and different metal electrodes. These contact resistances play a dominant role in electronic charge injection properties of OFETs, and therefore cannot be easily ignored when examining intrinsic properties such as mobility and its dependence on the temperature or the gate voltage. This chapter primarily examines how using various metals as the contacting electrodes affect the charge injection into OSCs. We divide this topic into linear vs. nonlinear charge injection. Linear contact resistances are seen in P3HT devices with a high metal work function, where the HOMO lies energetically close to the Fermi level of the injecting electrode. On the other hand, if there is a significant energy barrier between the two, nonlinear injection is observed.

The physics of charge injection at the metal/OSC contact in field-effect devices remains poorly understood. Contacts in OFETs (extremely restricted contact geometry, essentially undoped OSCs and large current densities due to the very thin channel thickness) are distinct from those in, for example, OLEDs (large contact areas, highly doped OSCs and smaller current densities). Different approaches have been developed to differentiate between contact and channel resistances, including analyses of single device characteristics [32, 14], scanning potentiometry [33, 34], gated four-probe measurements [50],

and scaling of total resistance with channel length in a series of devices [35, 36, 37, 38]. Several of these experiments have already shown that the parasitic series resistance, R_s, between the OSC and the metal electrodes can easily dominate the intrinsic channel resistance, R_ch, in short channel (few microns and below) OFETs [35, 36], and that R_s correlates inversely with mobility in polymer OFETs at room temperature [38].

As we discussed in Chapter 1, modeling of charge injection at the metal/OSC interfaces is a subject of much discussion [24]. Commonly used models include Schottky contacts [14] and antiparallel Schottky diodes in parallel with a resistance [35, 36]. More sophisticated treatments include the fact that conduction in disordered OSCs is by hopping [51], image charge effects [26], and account for charge recombination at the metal-OSC interface [52]. This last model has received recent experimental support in studies that examine scaling of the contact resistivity with mobility [38, 53].

Here, first we examine the results of our transport measurements in a set of OFETs with Au electrodes and P3HT as the active semiconducting polymer, with channel lengths from 400 nm to 45 μm. We determine the parasitic series contact resistance, R_s, and the true channel resistance, R_ch, from the dependence of the total source-drain resistance, R_on, on the channel length, L. Both R_s and R_ch increase as temperature is decreased, with R_ch varying more rapidly. The result is that the ratio $R_\mathrm{s}/R_\mathrm{ch}$ actually *decreases* as T is lowered; relative to the mobility, the contacts actually improve as T is decreased. More generally, we found that R_s correlates inversely with mobility over four decades, over a broad range of temperatures and gate voltages. We compare this data with the predictions of a recent theory [52, 53] of OSC/metal contacts incorporating a thermionic emission model with diffusion-limited injection currents and accounting for the backflow

of charge at the interface. Such a model predicts an inverse relationship between the mobility and the contact resistivity, provided that the Schottky barrier between Au and P3HT is low. This is expected to be the case since the HOMO of P3HT is estimated [18] to lie between 5.1 and 5.2 eV, close to the work function of Au (5.2 eV) [54].

In the case of lower work function metals such as Cr and Cu ($\sim$ 4.7 eV) [54], a significant Schottky energy barrier, Δ, for holes is expected to exist at the metal/OSC interface. For a channel mobility, μ, that is thermally activated with characteristic energy E_A, typically $<\sim$0.1 eV, the same model predicts a temperature dependence of the contact resistance, $R_s \propto \exp\left([E_A + \Delta]/k_B T\right)$. For $\Delta \sim 0.3$ eV, the temperature dependence of R_s is therefore predicted to be much stronger than the Au electrode case. However, in recent studies of charge injection in both bottom-contact P3HT FETs [54] and hole injection from a Ag electrode into poly-dialkoxy-p-phenylene vinylene [49], only a weak T dependence of contact resistance or injecting current was observed. These results imply that the diffusion-limited thermionic emission model is inadequate.

Work function differences may not be the only parameter determining the validity of thermionic emission models. However, experiments with systematic studies of similarly prepared devices made with identical OSCs and varying metals [54] imply that Δ is highly relevant to this question. In general, a simple thermionic or thermionic-diffusion model is not a realistic description of the injection process in these systems. The charge in these organic semiconductors is injected into and transported via a density of localized states that is strongly dependent on energy. The simple model of an activated over-barrier hop from the metal into a state in the semiconductor is inadequate, and the detailed energetics of the contact region must be considered. Only recently have the full temperature and

field dependence of the injection process been examined experimentally [54, 49].
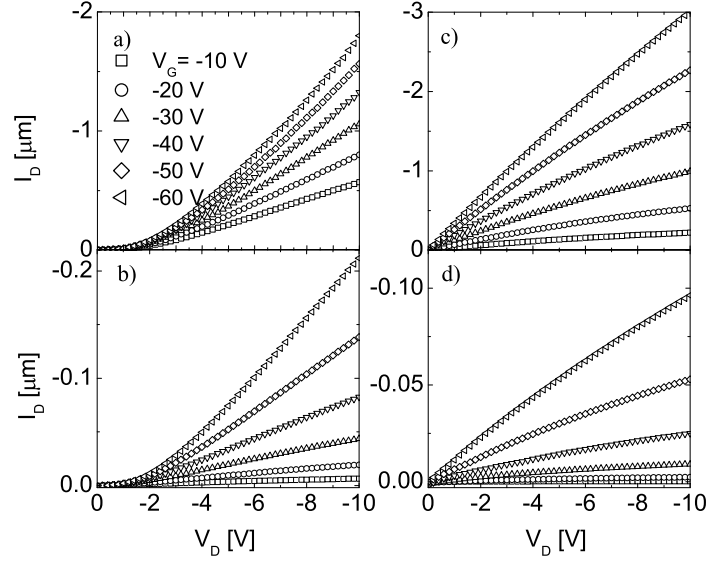
Figure 3.1: a) Transport characteristics ($I_D - V_D$) of a P3HT OFET with Cr source and drain electrodes, with $L = 25$ μm, $W = 200$ μm at 300 K for several gate voltages. b) Same device at 160 K. c) Analogous plot for a sample with Au electrodes of the same geometry, at 300 K and d) at 160 K.

With the presence of a significant Schottky injection barrier for holes in P3HT OFETs, the transport characteristics shows nonlinear behavior. Figs. 3.1a and (b) show $I_D - V_D$ of a P3HT OFET with Cr source and drain electrodes, with $L = 25$ μm, $W = 200$ μm at 300 and 160 K for several gate voltages. These plots are compared with linear transport in Au OFETs of the same geometry, in (c) and (d). The method of extracting R_s works well in devices where the OSC and the contacting metal electrodes form a linear Ohmic contact as seen in Au devices. In the case of nonlinear charge injection, one must consider the details of the relation between the injecting current and the contact voltage. To differentiate between the IV characteristics of the channel and the contacts, we examine the scaling

of device current with channel length, employ the gradual channel approximation [14], and divide the total source-drain voltage V_D into a channel component and a voltage dropped at the contacts, V_C. We assume, as supported by scanning potentiometry [54], that V_C is dominantly dropped at the injecting contact for metals with a significant Δ. We use $I_D - V_D$ data from a given series of devices of varying channel length, L, and fixed width, W, to extract both μ and $I_D - V_C$ for this metal/OSC interface. As expected, the $I_D - V_C$ characteristics of a specific interface are unique at a given T and V_G, independent of L. We analyze the field and temperature dependence of the injected current through a recent analytical model [26] of charge injection from a metallic electrode into a random hopping system. With reasonable fit parameters, this model agrees well with the observed temperature and field dependence of the injected current. We also discuss the distance scale over which V_C is dropped, and further experimental avenues to explore.

3.2 Experimental Details

As usual, devices are made in the bottom contact configuration (see for example Fig. 1.4) on a degenerately doped $p+$ silicon substrate used as a gate. The gate dielectric is 200 nm of thermal SiO_2. Source and drain electrodes are patterned using electron beam lithography in two different designs: One pattern is a series of L-shaped electrodes, with a fixed W and varying inter-electrode spacing (L), each separated from its neighbors by a distance of about one hundred microns. A second design is an interdigitated set of electrodes with a systematic increase in the distance between each pair. After a few months of experiments with the first design, we started to fabricate the subsequent samples in the interdigitated form. This pattern is more compact and allows for more device packing

per chip. In addition, it is easier to get uniform P3HT films across the interdigitated set, and therefore there are fewer fluctuations in performance from device to device. Three different kinds of metallic electrodes (Au, Cr, Cu) were then deposited by electron beam evaporation followed by lift off. (25 nm of each, preceded by 2.5 nm of Ti adhesion layer; no Ti layer for Cr samples). This thickness of metal is sufficient to guarantee film continuity and good metallic conduction, while attempting to minimize disruptions of the surface topography that could adversely affect polymer morphology. The P3HT solution was prepared and solution cast in the exact same manner as described in the previous chapter. Samples were all tested in vacuum, with HP4145B used for measurements.
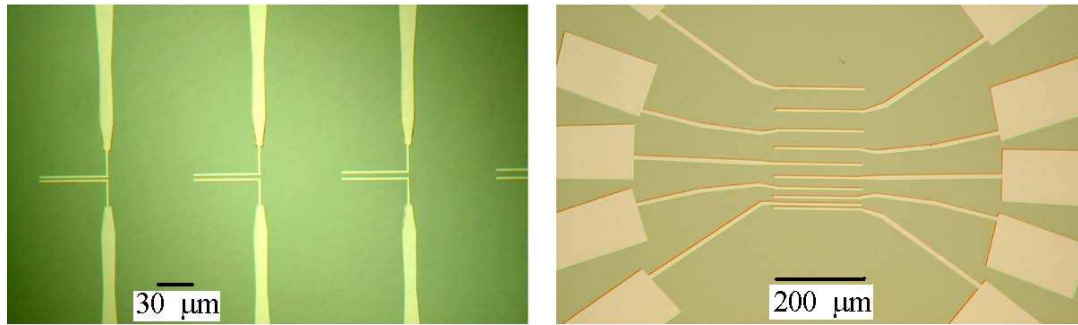
Figure 3.2: Two different sets of electrode patterns designed for the experiment. In both cases, the distance between each electrode increases systematically, while the channel width is kept fixed for all devices.

We found sample cleanliness to be of crucial importance to achieving devices with high quality, reproducible characteristics. Au electrodes were cleaned for one minute in a 1:1 solution of NH_4OH: H_2O_2 (30%), rinsed in de-ionized water, and exposed for about 1 min to oxygen plasma. The purpose of the oxygen plasma was to remove any remaining organic residue from the lithographic process.

The Cr samples were cleaned in the same manner followed by a last step dipping in

a buffered HF solution for under 10 seconds. The HF is believed to etch the native SiO_2 oxide, exposing a fresh layer of dielectric. Given the reactivity of Cr, it is natural to consider the importance of electrode oxidation. As was previously concluded by others [54], thin oxides appear not to affect transport significantly. For example, Cr electrode devices prepared by lift-off/O_2 plasma/HF dipping/P3HT deposition show transport properties very similar to those prepared by lift-off/HF dipping/O_2 plasma/P3HT deposition. This supports the conclusion that any small native oxide resulting from brief O_2 plasma exposure does not strongly influence device properties.

Cu electrodes were more problematic, and were only exposed to less than 25 seconds of O_2 plasma to clean the organic residue from the lift off. We found that Cu samples exposed to any cleaning procedure except for short O_2 plasma generally exhibited very poor transport properties. Without O_2 plasma exposure, mobilities were poor and contact resistances were higher, presumably due to remaining organic contaminants on the electrodes and the dielectric surface. Longer exposures to O_2 plasmas (greater than one minute) clearly resulted in the formation of a significant oxide layer, as indicated by discoloration of the electrodes. Exposure of Cu electrodes to HF never produced improved performance, and often resulted in poor transport (significantly reduced mobilities) compared to no-HF devices.

3.3 Linear Charge Injection

Here, we first discuss our findings in the case of linear charge injection in devices made from Au electrodes. We have observed that there are also several other metals that make Ohmic contacts to P3HT, such as platinum (Pt) and indium tin oxide (ITO). Here

Table 3.1: Parameters describing ensembles of devices analyzed in this study. Mobility values are obtained from $I_D - V_D$ data using Eq. (3.3.1). Contact resistivity values are computed by extrapolating R_{on} back to $L = 0$.

Ensemble width [μm]	min. L [μm]	max. L [μm]	μ_{FE} (300 K, $V_G = -90$ V) [cm^2/Vs]	$R_s W$ (300 K, $V_G = -90$ V) [Ω-cm]
5	0.4	5	0.73	1.1×10^3
30*	2	30	0.16	9.6×10^3
100	5	40	0.13	1.1×10^4
200*	5	45	0.11	1.79×10^4

*Data for the 30 and 200 μm wide devices were at $V_G = -70$ V rather than -90 V.

however, we analyze the Au/P3HT results only. We report data for four arrays, each with at least eight FET devices, with parameters as described in Table 3.1. For brevity, most of the data in subsequent figures are drawn from the $W = 5$ μm ensemble, and are representative of the other channel widths. For each device at each gate voltage, the linear portion of $I_D - V_D$ is used to find $R_{on} \equiv \partial I_D / \partial V_D$, the total source-drain resistance. The values of R_{on} are then plotted as a function of channel length for the ensemble of OFETs, as shown in Fig. 3.3 for two different sets of samples. The slope of such a plot describes R_{ch} per unit channel length. The intercept (the extrapolated resistance of a device of zero channel length) gives R_s, the total parasitic series resistance of the source and drain contacts. The true field-effect mobility, μ_{FE}, may be inferred from the gate voltage dependence of R_{on}:

$$\frac{\partial \left[\left(\frac{\partial R_{on}}{\partial L} \right)^{-1} \right]}{\partial V_G} = \mu_{FE}(V_G, T) W C_i, \tag{3.3.1}$$

where C_i is the capacitance per unit area of the gate oxide. Mobilities inferred from the saturation regime (*uncorrected* for contact effects) are systematically lower than corrected μ_{FE} values, and are comparatively independent of L. Device IV characteristics are stable with thermal cycling, and samples stored in vacuum for two months exhibit undegraded

performance.
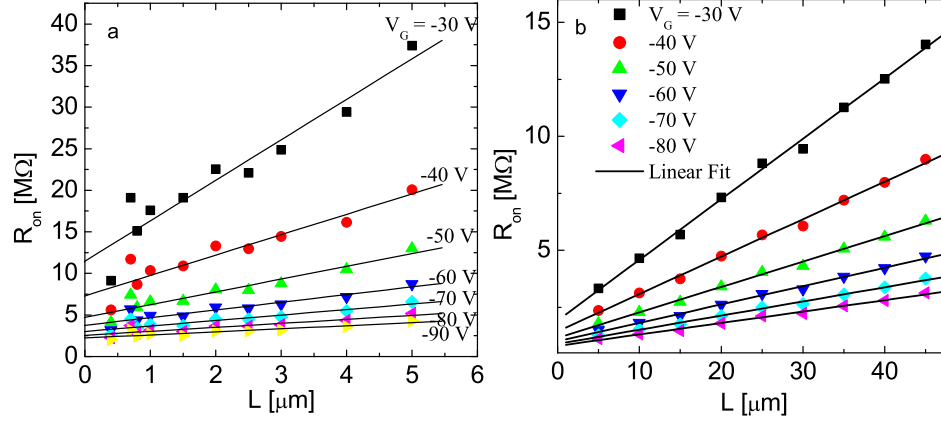
Figure 3.3: R_{on} as a function of L at 300 K for a series of Au/P3HT OFETs with channel widths of a) 5 μm. and b) 200 μm.

Figure 3.4a shows the temperature dependence of μ_{FE} for this series of 5 μm wide devices as a function of T^{-1}. The temperature dependence is well approximated as thermal activation, with the activation energy, E_A, weakly dependent on gate voltage. For $V_G = -90$ V, $E_A \approx 67.7$ meV; for $V_G = -30$ V, $E_A \approx 117$ meV.

The temperature dependence of the parasitic contact resistance for the same devices is shown in Figure 3.4b. The contact resistance increases significantly as T is decreased, again in an activated fashion. The activation energies are very similar to those for μ_{FE}, strongly suggesting that the same physics couples both these parameters. The activation energies inferred for R_s are systematically *below* those inferred for μ_{FE} for all gate voltages by a few meV (~ 4 meV for the 5 μm ensemble of devices).

A recently developed theory of metal/OSC contacts [52, 53] based on earlier work examining injection into poor conductors [25] suggests why this should be so. Scott and
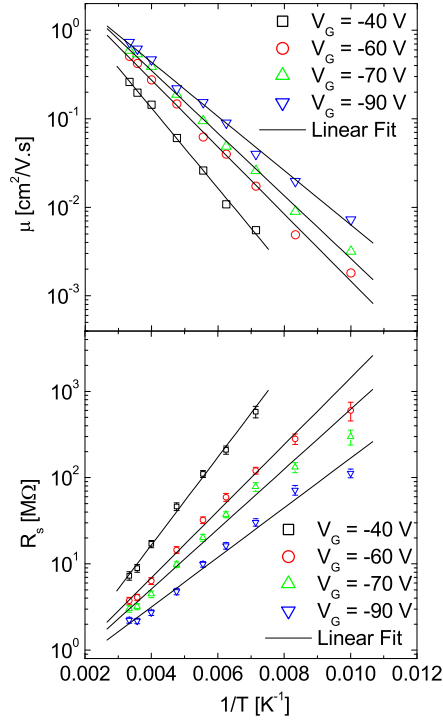
Figure 3.4: a) Mobility as a function of $1/T$ for several gate voltages, found via Eq. (3.3.1) in a series of 5 μm wide devices. Note the high values of μ_{FE} at large V_{G} and high T. b) Parasitic contact resistance as a function of $1/T$ for the same devices.

Malliaras [52] predict that the rate of injection into an OSC from a contact-limited metal electrode is proportional to the OSC mobility. In particular they show

$$J_{\text{INJ}} = 4\psi^2 N_0 e\mu F \exp(-\Delta/k_{\text{B}}T)\exp(f^{1/2}), \tag{3.3.2}$$

where ψ is a slowly varying function of electric field, F; N_0 is the density of localized sites available for hopping conduction; Δ is the Schottky barrier between the metal and the OSC; and the $f = e^3 F/[4\pi\epsilon\epsilon_0(k_{\text{B}}T)^2]$ term is due to Schottky barrier lowering. This variation of injection current density with OSC mobility has been confirmed in two-terminal metal/OSC diodes [53]. In the low field limit, if the mobility itself is thermally activated with a characteristic energy $E_{\text{A}}(V_{\text{G}})$, one would expect $R_{\text{s}} \propto \exp{(E_{\text{A}}(V_{\text{G}}) + \Delta)/k_{\text{B}}T}$.

The similarity of activation energies for R_s and μ_{FE} would follow naturally, provided that the Schottky barrier between Au and P3HT is low.
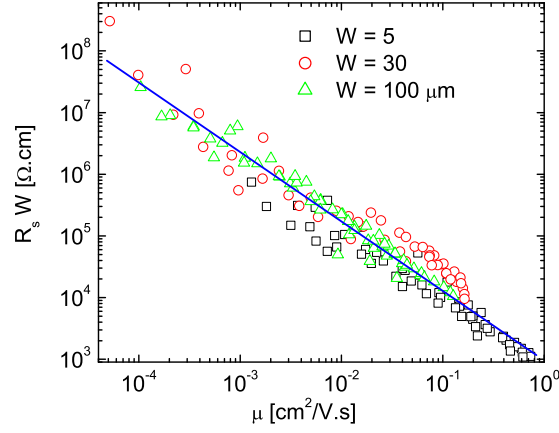
Figure 3.5: A summary plot of contact resistivity as a function of field-effect mobility, for all three ensembles of devices, and for all gate voltages and temperatures examined. Error bars have been omitted for clarity. The fit is to a power law with exponent -1.09.

Note that Eq. 3.3.2 implies that, for a given system at a fixed temperature, $R_s \propto 1/\mu_{FE}$. The constant of proportionality is temperature-dependent, and would be dominated by the Schottky barrier contribution, $\sim \exp(\Delta/k_B T)$. Figure 3.5 is a plot of $R_s W$ vs. μ_{FE} for three device ensembles, including data for all gate voltages and temperatures examined. The fit demonstrates that $R_s \sim 1/\mu_{FE}^{1.09}$ over *four decades* of mobility. This strongly supports the mobility dependence of the injection model of Eq. 3.3.2 derived in Ref. [52], provided the Schottky barrier for the Au/P3HT interface is nearly zero. Such a small barrier is consistent with the similarity in activation energies for R_s and μ_{FE} described above and seen in Fig. 3.4.

Fig. 3.6 shows the ratio of R_s to R_{ch} for a $L = 1$ μm device from the 5 μm wide
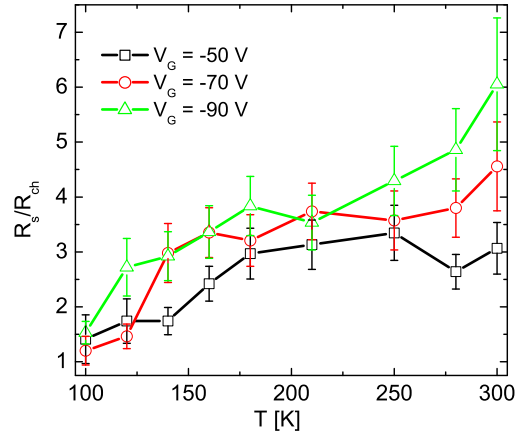
Figure 3.6: R_s/R_{ch} as a function of temperature for several gate voltages in the $W = 5$ μm devices, for a channel length of 1 μm. Relative to the channel, the contacts actually improve as the temperature decreases.

ensemble of devices as a function of temperature. Error bars are significant because of the uncertainty in the slope and intercept parameters obtained from data like that in Fig. 3.3. These errors are dominated by device-to-device fluctuations within the ensemble. The ratio decreases slowly as T is reduced. Within the model of Eq. (3.3.2), this suggests that the barrier height for our Au/P3HT interface is actually slightly negative, again consistent with the systematic difference in activation energies discussed above. Relative to the channel, the contacts actually *improve* slightly at low temperatures, so that a device that is bulk-limited at room temperature will remain so at lower temperatures.

3.4   Nonlinear Charge Injection

The technique of extracting R_s from the transport plots works fairly well in samples with Ohmic contacts to the OSC material such as the Au devices. In cases where a significant Schottky barrier is expected [54] to exist at the metal/OSC interface (such as

Cr or Cu/P3HT devices), the transport is nonlinear and one has to consider the details of charge injection at the contact, i.e., $I_D - V_C$. It is generally accepted [18, 26] that the size of Δ alone determines the nature of transport in a device, i.e., injection limited vs. bulk transport. In the following subsection, we explain our method of extracting the contact current-voltage characteristics, followed by interpretation and modeling of the data.

3.4.1 Extracting contact current-voltage characteristics

The injection properties of the contact can be examined [14] by splitting the channel into two regimes of contact and the main channel (See Fig. 3.7). A voltage of V_C is dropped
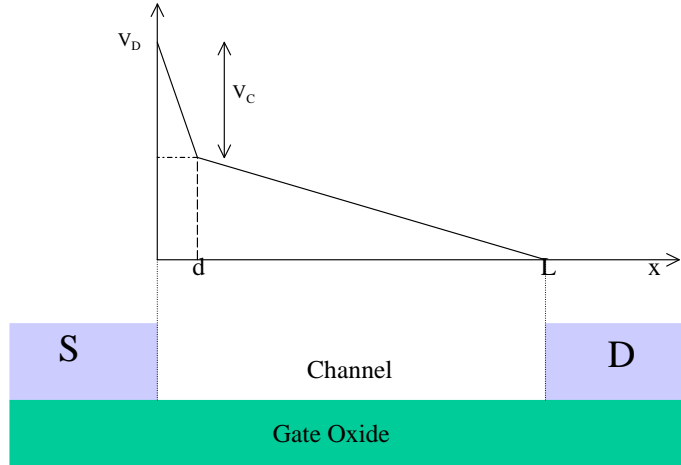
Figure 3.7: A cartoon demonstrating the simple model of gradual channel approximation used in the analysis to exact the contact current-voltage characteristics.

across the contact with the remaining $V_{ch} = V_D - V_C$ across the main channel. Using the charge control model [12], I_D is given by 1.2.1:

$$I_D = W C_i \mu [V_G - V_T - V(x)] \frac{dV}{dx}, \qquad (3.4.1)$$

where $V(x)$ is the potential in the channel at some position x, V_T is the threshold voltage, C_i is the capacitance per unit area of the gate dielectric, and μ is the intrinsic channel mobility. Integration of Eq. 1.2.1 from $x = 0$ to $L - d$ gives:

$$\frac{I_D}{W C_i \mu}(L - d) = (V_G - V_T)(V_D - V_C) - \frac{1}{2}(V_D^2 - V_C^2), \qquad (3.4.2)$$

where V_C is dropped across d, a characteristic depletion length near the contacts. In this treatment, we assume V_C to be entirely dropped across the injecting contact. Scanning potentiometry experiments in this material [33, 34, 54] have previously shown that, in systems with significant Δ, most of the potential drop due to contacts occurs at the source, where holes are injected into the channel.

Eq. 3.4.2 can be used to extract a value of V_C for any pair of (V_D, I_D) data, though there is no independent way of knowing the correct value of μ. With an array of devices, one can use the length dependence of I_D to address this difficulty. At a given T and V_G, a series of $I_D - V_D$ data is collected from devices with different channel lengths. The corresponding $I_D - V_C$ is calculated from Eq. 3.4.2 for all the different L. If the contact and channel transport properties in each device are identical, the correct value of μ would make all the different $I_D - V_C$ curves collapse onto one, since the injection characteristics of a particular OSC/metal interface should be unique and set by material properties and the (fixed) channel width and electrode geometry. This technique allows for the simultaneous extraction of μ and $I_D - V_C$. Since the average source-drain field in our devices is low ($< 10^3$ V/cm), no significant field dependence of μ is expected [14] or observed.

To confirm this method of extracting μ and $I_D - V_C$, we fabricated a series of devices
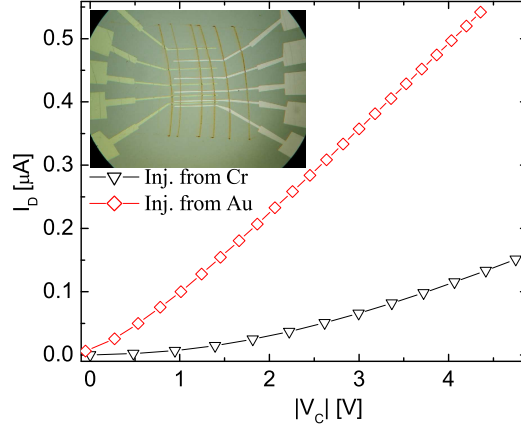
Figure 3.8: Extracted $I_D - V_C$ for a series of devices of width 200 μm with alternating Cr and Au electrodes at 240 K and $V_G = -80$ V. Upper curve shows injection of holes from Au, while lower curve shows injection from Cr. Injection from Au is more linear and allows higher currents at lower voltages. The Au data have been shifted to lower $|V_C|$ by 0.5 V to account for a small contact voltage at the drain. Inset: Top view of alternating Au (left) and Cr (right) electrodes. The P3HT film can be seen at the center of the pattern.

(in a two-step lithography process) with *alternating* Au and Cr electrodes. A device of this configuration has been shown in the inset of Fig. 3.8. The data is then taken twice for each device, once with the source electrode on Cr with the drain on Au and the second time *vice versa*. Fig. 3.8 shows a plot of extracted $I_D - V_C$ for injection from Cr and Au at $T = 240$ K and $V_G = -80$ V. We noticed that there is still a minute nonlinearity present in data for Au at that is not present in all-Au devices. We believe that this is consistent with a small contact voltage at the drain, as was seen in the potentiometry profile of Cr/P3HT devices in Ref. [54]. The Au data in Fig. 3.8 have been shifted toward lower $|V_C|$ by 0.5 V to account for this. The value of μ that collapses the different length-dependent data for injection from Cr onto one $I_D - V_C$ curve is *identical* to that

inferred from the length-dependence of the channel resistance when injection is from Au in the same devices. This demonstrates that this procedure of extracting $I_D - V_C$ is well-founded.

The mobilities in the Au/Cr devices are lower than those seen in all Au or all Cr source/drain samples (discussed below). We believe this to be due to inferior surface cleanliness of samples made in the two-step lithography technique. The contact resistance data for injection from Au agree *quantitatively* with the data observed in Fig. 3.5.
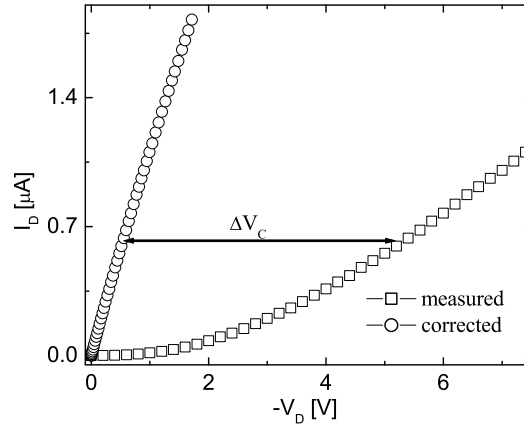
Figure 3.9: Measured $I_D - V_D$, and the same data corrected for contact voltages (*i.e.* $I_D - V_{ch}$) for the Cr electrode device shown in Fig. 3.1, at 290 K and $V_G = -60$ V. The device is clearly quite contact limited.

Fig. 3.9 shows a plot of measured $I_D - V_D$ and the current corrected for contact voltages, *i.e.* $I_D - V_{ch}$, for the all-Cr sample described above at $V_G = -60$ V. As seen from the plot, most of the total voltage is dropped across the contact, making these devices severely contact limited. For example, for a drain voltage of 2 V, $V_C/V_{ch} \sim 30$.

Fig. 3.10a shows the temperature dependence of μ extracted this way as a function of
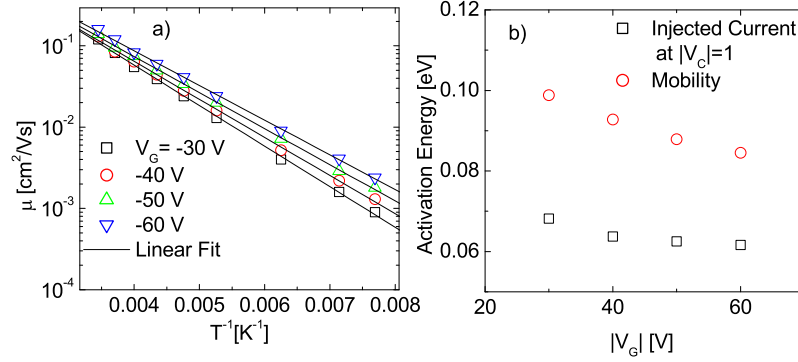
Figure 3.10: a) Temperature dependence of the extracted channel mobility as a function of T^{-1} for a set of devices with Cr source and drain electrodes at several gate voltages. b): Activation energies of the injected current and E_A as a function of V_G.

T^{-1} for a set of devices with all-Cr source/drain electrodes. The temperature dependence is well approximated as thermal activation consistent with simple hopping of carriers between localized states in the channel. The activation energies E_A for the mobility are quantitatively similar to those seen in all-Au devices. Fig. 3.10b shows that the activation energies of the injected current (at $V_C = 1$ V) are *smaller* than E_A. In agreement with others' results [54, 49], this is *inconsistent* with the simple thermionic-diffusion model of injection. As discussed in the next section, the hopping injection model predicts this weak temperature dependence.

A similar plot for the temperature dependence of channel mobility in a sample with Cu source/drain electrodes is shown in Fig. 3.11a. The values of μ in Cu devices are consistently lower than those seen in Cr or Au, though the activation energies are very similar. The reason for these lower mobilities remains unclear, since contact effects have been accounted for. However, it is commonly observed [54, 55] that the field effect
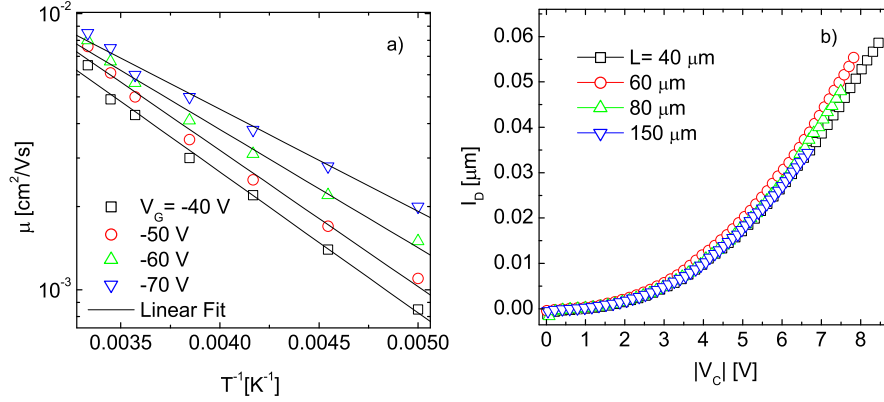
Figure 3.11: a) Temperature dependence of the extracted channel mobility as a function of T^{-1} for a set of devices with Cu source and drain electrodes at several gate voltages. b): An example of "collapsed" $I_D - V_C$ data for devices of different values of L with Cu electrodes, $W = 400$ μm, 240 K, $V_G = -70$ V.

mobility can be significantly different in nominally identically prepared samples. The values of contact resistivity, $R_s W$ are also higher in Cu devices. At a small $V_s \sim 1$ V, $R_s W$[Cu] $\sim$3300 kΩ-cm, while the corresponding value for Cr is $R_s W$[Cr] $\sim$125 kΩ-cm. For devices with Au source/drain electrodes, $R_s W \sim 10$ kΩ-cm was obtained, as seen in table 3.1. The increase in contact resistivity from Au to Cu is consistent with the increase in value of Δ as described below. Fig. 3.11b shows an example of a coalesced plot of $I_D - V_C$ for different values of L for the Cu sample at $T = 240$ K and $V_G = -70$ V. A single mobility value of 3.8×10^{-3} cm^2/V.s was used to obtain this collapse.

Finally, it should be mentioned that this procedure of extracting the contact current-voltage characteristics works also fairly well in Au/P3HT devices, where transport is linear. Fig. 3.12 shows a plot of extracted $I_D - V_C$s for a Au sample with $W = 200$ μm and different gate voltages at $T = 250$ K. From this graph, it can be seen that the relationship between the current and the contact voltage is linear, consistent with the
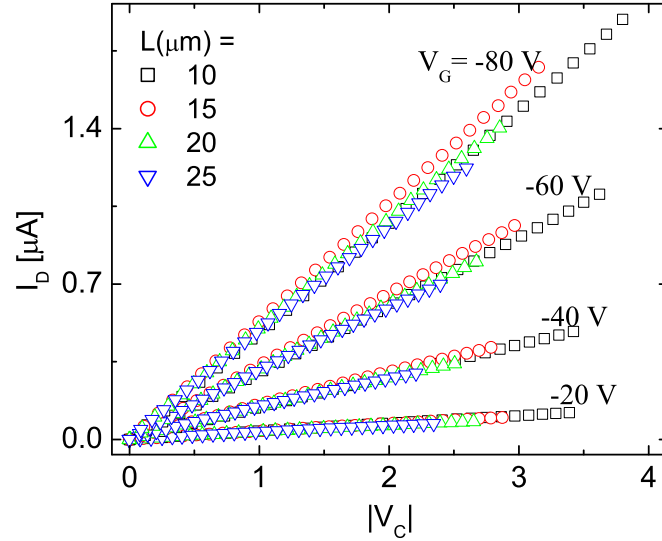
Figure 3.12: Contact current-voltage characteristics for the Au sample described in Fig. 3.3b at $T = 250$ K. At any given V_G, the data for different channel lengths is collapsed onto one, using an appropriate value for μ. Therefore, the $I_D - V_C$ data is unique for any V_G and T

presence of only a negligible energy barrier at the Au/P3HT interface. Also, as expected, we find the device parameters such as the contact resistance and the mobility are the same as those obtained from R_{on} vs. L analysis.

3.4.2 Interpretation and modeling

Having extracted nonlinear current-voltage characteristics for the injecting contacts, we analyze the resulting data in terms of a particular model of injection into disordered polymer semiconductors. As mentioned earlier, the diffusion thermionic models are insufficient to account for the weak temperature dependence of the observed injected current. The analytic treatment by Arkhipov *et al.* [26] of charge injection from a metallic electrode into a random hopping system has been shown [49, 56] to consistently explain the field and

temperature dependence of charge injection in organic Schottky diode-like structures. In this picture, the weak temperature dependence of the injection current is a consequence of a Gaussian distribution of states [57]. Therefore the injection process is easier at lower temperatures, leading to a weaker temperature dependence of the current. Here we apply Arkhipov's results to our charge injection data in OFETs and show that this treatment, with reasonable parameters, is consistent with the measured data.

The key to this analysis is the conclusion [54, 58] that a small depletion region forms in the vicinity of the contacts, and that V_C is dropped across this region at the injecting contact. We note that the values of V_C can be as large as a few volts. Establishing the distance scale, d, relevant to converting this into the electric field at the contact is nontrivial, though reasonable bounds may be placed on this parameter. The resolution of existing scanning potentiometry data in similar OFET structures [34, 54] establishes that d cannot exceed ~ 400 nm. Furthermore, the lack of breakdown or irreversible device damage implies that the injecting field must be below the breakdown field of the OSC, so that d must be larger than ~ 10 nm. After presenting the analysis of the $I_D - V_C$ data, we return to this issue below.

In this 1d model [26], the transport of carriers takes place in a hopping system of Gaussian energy distribution in close contact with the metallic electrode. This density of states (DOS) is given by:

$$g(E) = \frac{N_t}{\sqrt{2\pi}\sigma} \exp\left(-\frac{E^2}{2\sigma^2}\right), \qquad (3.4.3)$$

where N_t is the total spatial density of localized states, with σ as the variance of the Gaussian distribution centered about $E = 0$. The emphasis is placed on the primary

injection event where a carrier from the metal is injected into a localized state a distance $x_0 > a$ from the interface, where a is the intersite hopping distance. The potential of this carrier at any distance x from the interface is given by

$$U(x, E) = \Delta - \frac{e^2}{16\pi\epsilon_0\epsilon x} - eF_0 x + E, \qquad (3.4.4)$$

where Δ is the energy difference between the Fermi level of the metal and the center of DOS in the semiconductor, F_0 is the external field at the contact, e is the elementary charge, and ϵ is the relative dielectric constant of the polymer. Once a carrier is injected into a localized state in the polymer, it can either go back to the metal due to the attractive image potential, or escape with a finite probability to diffuse into the bulk. The escape probability can be solved using the 1d Onsager problem as outlined in detail in Ref. [26]. The final result predicts the injection current density as follows:

$$
\begin{aligned}
J_{\text{inj}} \;=\; & e\nu \left(\int_a^\infty dx \exp\left[-\frac{e}{k_{\text{B}}T} \left(F_0 x + \frac{e}{16\pi\epsilon_0\epsilon x} \right) \right] \right)^{-1} \times \\
& \int_a^\infty dx_0 \exp(2\gamma x_0) \int_a^{x_0} dx \exp\left[-\frac{e}{k_{\text{B}}T} \left(F_0 x + \frac{e}{16\pi\epsilon_0\epsilon x} \right) \right] \times \\
& \int_{-\infty}^\infty dE' \text{Bol}(E') g[U(x_0) - E'].
\end{aligned}
\qquad (3.4.5)
$$

Here, ν is the attempt-to-jump frequency, T is the temperature, γ is inverse localization length, and the Boltzmann function $\text{Bol}(E)$ is defined as:

$$
\begin{aligned}
\text{Bol}(E) \;=\; & \exp(-E/k_{\text{B}}T), E > 0, \\
\;=\; & 1, E < 0.
\end{aligned}
\qquad (3.4.6)
$$

To apply this model, we first need to fix the parameters σ, a, and γ. It is possible to extract σ from a model of carrier transport in a disordered Gaussian density of states [59,

Table 3.2: Parameters used to model the $I_{\rm D} - V_{\rm C}$ data of this study within the charge injection treatment of Ref. [26] for all T. The relative dielectric constant ϵ of the polymer was assumed to be 3. At each gate voltage a single numerical prefactor was the only necessary adjustment.

Contact metal	σ [eV]	a [nm]	γ [nm^{-1}]	Δ [eV]	d [nm]
Cr	0.046	1.6	4.35	0.23	150
Cu	0.046	1.6	4.35	0.31	230

60] by plotting $\ln(\mu_0)$ vs. T^{-2}, where μ_0 is the value of the zero-field mobility. We note that our data appear to be better described as exponential in T^{-1} rather than T^{-2}; nonetheless this procedure provides an estimate for a value of σ. Calculation of the values of a and γ [59] can be difficult, as one has to use the strong field dependence of mobility. As mentioned earlier, our data are acquired in a low enough source-drain average field that no field-dependence of μ may be inferred. Therefore, we chose a and γ consistent with reported values in literature [59] or previous experiments (i.e., values extracted from Vissenburg fits discussed in Chapter 2.). We note that changing a or γ over a reasonable range mainly affects the overall prefactor of the current (as described below), without significantly altering the shapes of the predicted curves.

With σ, a, and γ held fixed, the only parameters that can be adjusted to fit Eq. 3.4.5 to a plot of data are Δ, a prefactor $K \equiv A\nu N_{\rm t}$ (where A is an effective injection area), and d, where $F_0 = V_{\rm C}/d$. We observed, as discussed in detail in Ref. [26], that the nonlinearity in a plot of $I_{\rm D} - V_{\rm C}$ is mainly controlled by the value of Δ and the strength of the electric field. At $F_0 \sim 5 \times 10^7$ V/m or higher, the plots are severely nonlinear and the temperature dependence of the current would be extremely weak. At lower fields, the nonlinearity is less severe and the temperature dependence is stronger. Therefore, the

value of d is paramount, and constrained as described above.
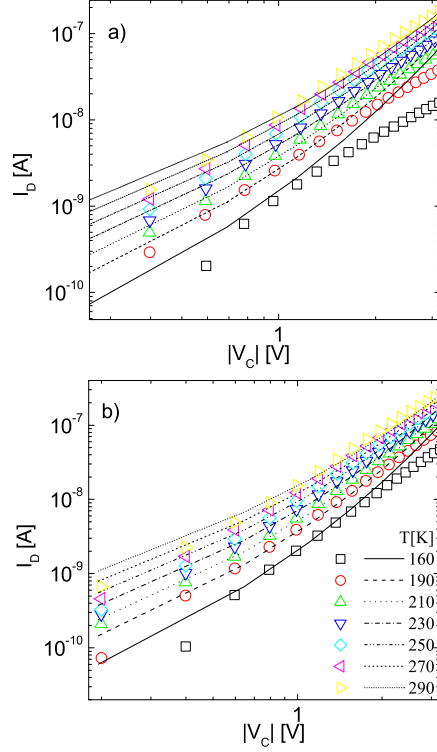
Figure 3.13: $I_D - V_C$ data from a set of Cr electrode devices, together with curves from the model of Eq. 3.4.5 at gate voltages (a) -30 V, and (b) -60 V.

Having expected $\Delta \sim 0.3$ eV, we find that d cannot be below 100 nm within this model; the resulting large values of injecting field F_0 would yield temperature and field dependences inconsistent with those observed. Table 3.2 summarizes the parameters used to model the injection data for both all-Cr and all-Cu sets of devices. Figures 3.13a and b show plots of $I_D - V_C$ and the corresponding numerical integration of Eq. 3.4.5 using parameters given in Table 3.2 (with an appropriate value of prefactor K) for injection from Cr over a representative range of temperature for gate voltages -30 V and -60 V.

Fig. 3.14 shows the temperature dependence of the injected current in low V_C regime and the Arkhipov fit to the data. Notice that the predicted temperature dependence in the diffusion thermionic model is much stronger than the Arkhipov model if the same $\Delta = 0.23\,\text{eV}$ is used. Fig. 3.15 shows a plot of $I_D - V_C$ for a Cu sample at $V_G = -60\,\text{V}$. The fit to the data is valid only in the low V_C regime as saturation effects in the transistor start to affect $I_D - V_D$ data at large V_D. Note that the procedure outlined above to extract the $I_D - V_C$ data assumes that devices are firmly in the gradual channel limit, with no saturation effects. Also, the effects of leakage currents to the gate electrode in the immediate vicinity of $V_C = 0$ at low temperatures can be seen in Figs. 3.13 and 3.15.
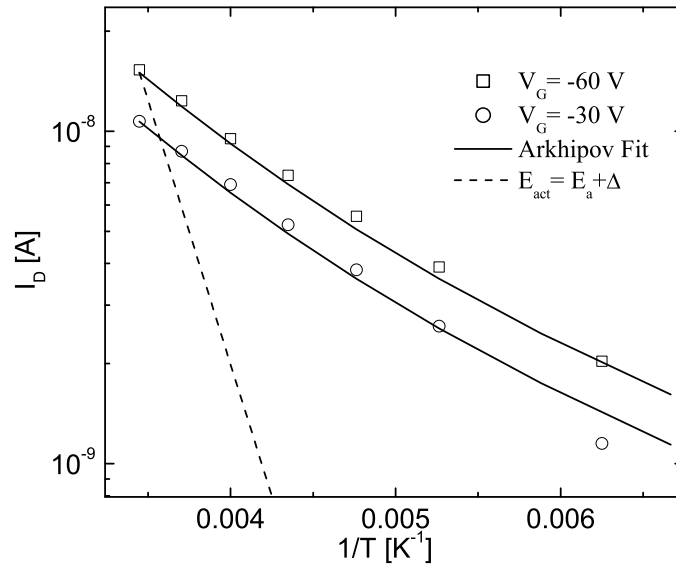
Figure 3.14: Temperature dependence of the injected current for Cr electrodes at low V_C, with Eq. 3.4.5 fits to the data. The dashed line shows the predicted T dependence of the thermionic diffusion model for the same value of Δ.
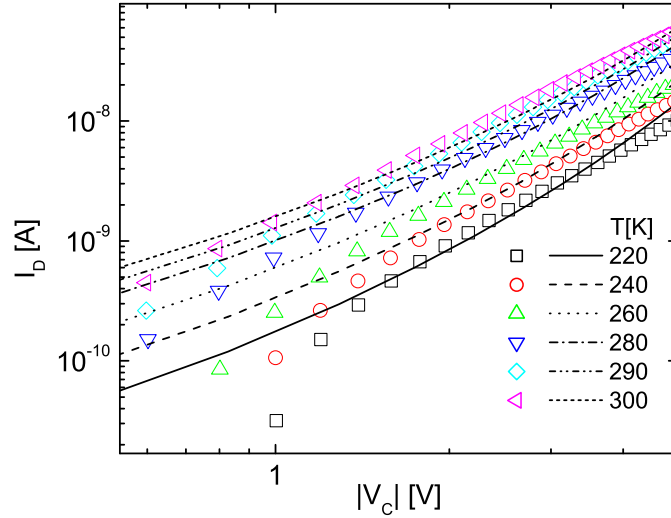
Figure 3.15: $I_\mathrm{D} - V_\mathrm{C}$ for devices with Cu electrodes ($W = 400$ μm) at $V_\mathrm{G} = -60$ V over a representative temperature range, together with results from Eq. 3.4.5 and the parameters of Table 3.2.

N_t is the only gate-dependent parameter in this model. The parameters listed in Table 3.2 are kept fixed for all temperatures and all gate voltages. Since the prefactor in Eq. 3.4.5 is the product $A\nu N_\mathrm{t}$, it is therefore not possible to determine an exact value for just N_t. For a cross-sectional area of injection of $A \sim 25$ nm$\times 2 \times 10^5$ nm and $\nu \sim 10^{13}$ s^{-1}, we find $N_\mathrm{t} \sim 1.1 \times 10^{22}$ cm^{-3} for $V_\mathrm{G} = -60$ V and $N_\mathrm{t} \sim 8.3 \times 10^{21}$ cm^{-3} for $V_\mathrm{G} = -30$ V. These values are consistent with other experiments [49, 56].

Table 3.2 shows that the obtained injection barrier height for copper is about 80 meV higher than that for Cr. This difference in the barrier energy is not unreasonable, and may be attributed [54] to an interfacial dipole layer at the interface changing Δ by a small amount. *In-situ* ultraviolet photoemission spectroscopy measurements would be well-suited to testing this hypothesis [61, 62, 63]. The higher injection barrier for copper is

consistent with the observed higher contact resistivity and lower overall currents observed in Cu.

The length of the presumed depletion region is also a bit higher in Cu samples (by ~ 80 nm), though it does not necessarily reveal why the mobility is lower in these devices. The origin of these depletion regions in the vicinity of the contacts is not understood in detail. Recent 2d electrostatic modeling [58] of OFETs has shown that the effect of significant energy barriers at the injecting electrode is formation of regions of low carrier concentration (and mobility) near the contacts. These studies place the extent of these regions at about 100 nm from the contact, depending on V_{G}. Another possible origin for regions of reduced mobility near metal contacts with significant barriers is charge transfer and band bending near the interface. Since conduction in these materials can be treated as percolative variable range hopping [23], μ is a natural function of the density of available hopping sites. The occupation of those sites can be strongly modified by interfacial charge transfer between the metal and the OSC. Improved local probes (nm-resolution scanning potentiometry, cross-sectional scanning tunneling microscopy) would be extremely useful in better understanding these depletion regions.

One can question the validity of this hopping injection model in the limit where $\Delta \rightarrow 0$. In fact, in this model the presence of space charge effects are ignored in the vicinity of the contact. This means that the potential energy given by Eq. 3.4.4 at $x = a$ must be positive [26], constraining $\Delta > F_0 a + \frac{e^2}{16\pi\epsilon_0\epsilon a}$. For a range of typical values, one finds that the Arkhipov treatment is valid for $\Delta \gtrsim 0.2$eV. Therefore, this model cannot be appropriately used to interpret the linear charge injection data observed in Au/P3HT devices. In this case, the picture of drift/diffusion of carriers and a mobility

dependent charge injection as discussed earlier seems to be more valid. V. I. Arkhipov has acknowledged, through private correspondence with us, that a more complete analysis of the hopping model should reduce it down to the drift/diffusion results in the limit of small Schottky energy barriers, but at this moment such treatment is lacking.

3.5 Conclusions

Transport properties of a series of organic field-effect transistors with P3HT as the active polymer layer and Cr, Cu and Au as the source/drain electrodes were examined over a temperature range. In Au/P3HT devices where linear transport is observed, we used the length dependence of the channel resistance to extract the intrinsic mobility and parasitic contact resistance as a function of temperature and gate voltage for several series of OFETs. Our data were consistent with a mobility-dependent charge injection model accounting the backflow of charge at the interface. We find that the ratio of contact to channel resistance actually decreases slightly as T is reduced, making the devices channel-limited at lower temperatures. Once parasitic contact resistances are taken into account, the mobility of solution-cast P3HT can approach 1 cm^2/Vs at room temperature, nearly an order of magnitude larger than uncorrected mobilities. These results indicate that performance of P3HT-based OFETs can be limited more by contact physics than by the intrinsic transport physics in the polymer itself. For the case of nonlinear charge injection from Cr and Cu electrodes, a general approach, incorporating the graduate channel approximation and scaling with length of the conductance, was used to extract the contact current-voltage characteristics of the different devices, with the assumption that the injection barrier primarily applies to holes being injected from

the source. This procedure was checked for consistency using devices with electrodes of alternating metal composition. The data confirm that the weak temperature dependence of the injected current cannot be simply explained using the general diffusion-thermionic emission models. With reasonable values of parameters, a more sophisticated model of hopping injection into a disordered density of localized states, with emphasis on the primary injection event, is consistent with the field and the temperature dependence of the data over a broad range of temperatures and gate voltages.

Chapter 4

INFLUENCE OF IMPURITY DOPANTS ON CHARGE INJECTION IN ORGANIC FIELD-EFFECT TRANSISTORS

4.1   Introduction

Charge injection from metallic electrodes into organic semiconductors is influenced by several factors such as metal work function, surface treatment, and doping levels. In the previous chapter, we investigated the process of charge injection from several metals (Au, Cr and Cu) into P3HT OFETs and showed that depending on the size of the energy barrier at the metal/OSC interface, linear or nonlinear transport is observed. Linear (Ohmic) $I - V$ characteristics is observed for injection from metals with sufficiently high work functions (i. e., Au, Pt, ITO or Pd with work functions $\geq$ 5.0 eV). However, in the process of experimenting with these devices, we noticed that the nature of charge injection for devices such as Au/P3HT or Pd/P3HT significantly changes upon annealing the OFETs in vacuum at elevated temperatures for a period of time. After several annealing steps, the normally linear transport for Au/P3HT devices becomes severely nonlinear. Since annealing has been known to reduce the concentration of background impurity dopants in the OSC, it's obvious that dopant density strongly influences the magnitude and mechanism of charge injection into OSCs. A doping-dependent charge injection study [64] into P3HT using planar and sandwich geometries has indicated that there are severe contact limitations at low doping densities. Hosseini et. al. have also

shown [65] that contact resistance in disordered OSCs significantly decreases at high doping concentrations due to dopant-induced broadening of the Gaussian density of localized states.

In this chapter, we examine doping-dependent charge injection in a series of (bottom-contact) OFETs using Au and Pt as the contacting electrodes and P3HT as the usual active organic polymer, and find an additional effect of doping. From the length dependence of the total device resistance, R_{on}, we extract the contact and channel resistances as a function of the gate voltage, V_G, and doping. Exposure to air and humidity is known to enhance hole doping in P3HT [66]. As we reduce the concentration of such dopants (related to the bulk P3HT conductivity) by annealing devices in vacuum at elevated temperatures, R_s and the ratio R_s/R_{ch} increases dramatically for Au/P3HT devices, with injection becoming non-Ohmic. For Pt/P3HT devices, R_s remains relatively low compared to R_{ch}, and injection remains Ohmic even when bulk conductivity is reduced below measurable limits.

Ultraviolet photoemission spectroscopy (UPS) is a useful tool to investigate energetic changes in the electronic band structure of interfaces. Since our transport data was consistent with formation of injection barriers, specially in Au/P3HT devices, we collaborated with Prof. Yongli Gao's research group at University of Rochester to test this hypothesis in both Au/P3HT and Pt/P3HT samples through UPS measurements. The experiments reveal that changing dopant concentration strongly alters the band alignment between the metal Fermi level and the OSC valence band. As dopants are removed, the energetic difference between the Au Fermi level and the P3HT valence band increases by about 0.5 eV, while this effect is much less severe in Pt/P3HT. These results demonstrate that

doping effects on surface dipole formation, charge transfer at the metal/organic interface, and band bending must be considered in any full treatment of metal/OSC charge injection.

4.2   Experimental Details

The fabrication of the transistors was described in great detail in the Experimental section of chapter three. The electrode pattern used for these measurements is the interdigitated set shown in Fig. 3.2, with $W = 200$ μm and L ranging from 5 to 45 μm. The cleaning procedure of the substrate prior to deposition of P3HT involved only a 2 min oxygen plasma. The weight concentration of P3HT in chloroform for this batch was 0.06%. The samples were immediately transferred to the vacuum probe station (10^{-6} Torr) following the deposition.

To produce a certain doping level, the sample is annealed at elevated temperatures ($\sim$350-380 K) in vacuum for several hours and then cooled down to room temperature for measurement. We characterize the doping by the effective conductivity, calculated from the low V_{D} source-drain conductance and the estimated P3HT layer thickness at zero gate voltage. In the absence of band bending at the P3HT/SiO$_2$ interface, there should be no "channel" at the interface, and the measured source-drain conductance should be a bulk effect. We note that similar conductances are found in two-terminal planar devices fabricated on glass substrates. The conductivity after an annealing step remains stable in vacuum at room temperature and below on the timescale of the measurements, indicating no further change in doping.

For the UPS measurements, samples were prepared by solution casting of P3HT on

thin films (25 nm) of Au or Pt using the same procedures as in the FET devices. The samples were then placed securely in small boxes and sent to University of Rochester for UPS analysis. Details of the UPS setup can be found in Ref. [67].

4.3 Results and Discussion

In what follows, we discuss our results of transport characteristics of Au and Pt OFETs as a function of annealing (dedoping) at high temperatures. Then in section 4.3.2, we present the UPS data collected by Huanjun Ding from Univ. of Rochester and discuss the significance of its findings in relation with our transport data.

4.3.1 The transport characteristics after annealing steps

Figure 4.1a shows the transport characteristics of a Au/P3HT device with $L = 10$ μm at $T = 300$ K and at a fixed $V_{\mathrm{G}} = -60$ V for different doping levels. Table 4.1 shows the annealing schedule for the Au/P3HT and Pt/P3HT devices. After the fourth annealing step source-drain transport in the Au/P3HT devices was highly nonlinear. In contrast, Fig. 4.1b shows a similar plot for a Pt/P3HT device with identical parameters as Au above. After a more extensive annealing process such that bulk P3HT conductivity was reduced below measurable limits, the $I_{\mathrm{D}} - V_{\mathrm{D}}$ data remain nearly linear. To ascertain whether the annealing process irreversibly alters the polymer or the interface, Au/P3HT samples exposed to ambient air were re-examined after several days, and the conductivity had returned to its initial pre-annealing levels. We carried out an additional annealing stage at this point (A.5*), which reproduced the nonlinearity trend observed earlier.

From the data in Fig. 4.1, we extracted R_{ch} and R_{s} from the L dependence of the total device resistance, $R_{\mathrm{on}} \equiv \partial V_{\mathrm{D}}/\partial I_{\mathrm{D}}$ as described in section 3.3. Figure 4.2a shows the
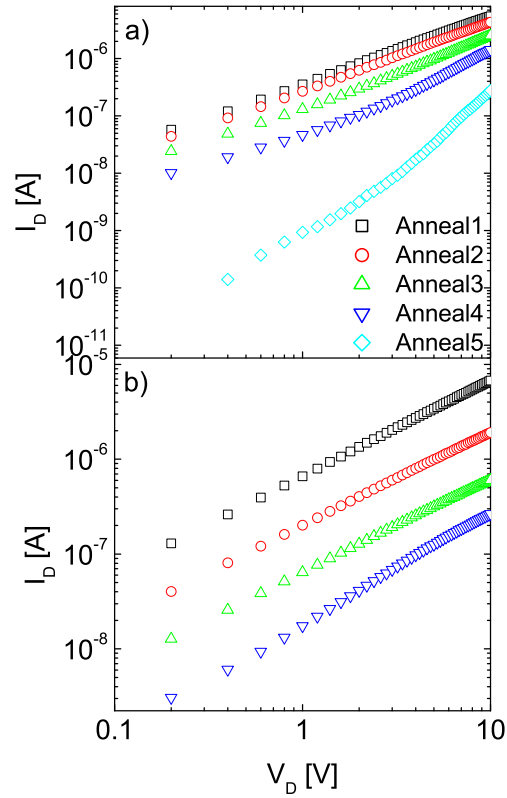
Figure 4.1: a) Log-Log plot of the transport characteristics of a Au/P3HT device with $L = 10$ μm at $T = 300$ K and at a fixed $V_{\mathrm{G}} = -60$ V for different annealing as described in the text. b) Similar plot for a Pt/P3HT device with identical geometry as (a).

V_{G} dependence of R_{s} for different annealing steps for the Au device at room temperature. Here we obtain R_{s} in the limit $|V_{\mathrm{D}}| < 1$ V, where transport is still reasonably linear even at higher dedopings. We note that we have developed a procedure for extracting contact current-voltage characteristics even in the limit of strong injection nonlineari-ties(see subsection 3.4.1) , but it is difficult to quantify such injection by a single number such as R_{s}. After each anneal, the contact resistance increases significantly. To test for contact-limited transport, we plot the ratio $R_{\mathrm{s}}/R_{\mathrm{ch}}$ as a function of V_{G} for a Au device

Table 4.1: Annealing times and temperatures and resulting bulk P3HT conductivities (for average film thickness of 25 nm). For Pt devices bulk conduction following the third and fourth anneals was below detectable limits. A.5* was performed after a few days of air exposure.

	stage	time (hrs)	T (K)	σ (S/m)
Au	anneal (A).1	17	350	0.032
	A.2	+7	350	0.022
	A.3	+12	350	0.0077
	A.4	+22	350	8.9×10^{-4}
	A.5*	16	370	-
Pt	A.1	24	350	0.064
	A.2	+17	360	0.0036
	A.3	+22	370	-
	A.4	+22	380	-

with $L = 10$ μm in Fig. 4.2b. At higher dedopings and higher gate voltages, the devices are clearly contact limited. Thus the nonlinear transport seen in this regime at higher biases indicates the possible formation of a charge injection barrier for holes. Analogous data for Pt devices (not shown) reveals that the contact resistance is lower than that observed for Au, and that R_s/R_ch remains below 1, only reaching approximately 1 at the most severely dedoped levels.

To further confirm that charge injection from Au electrodes becomes more difficult at lower doping levels than injection from Pt, we fabricated a series of devices (in a two-step lithography process) with *alternating* Au and Pt electrodes. The data are taken twice for each device, once with the source electrode on Au with the drain on Pt and the second time vice versa. At higher doping levels, the transport data are similar for injection from Au and Pt, but as the sample is annealed, injection from Au becomes more nonlinear and allows for less current at low drain biases. Fig. 4.3 shows a linear plot of $I_\text{D} - V_\text{D}$ for
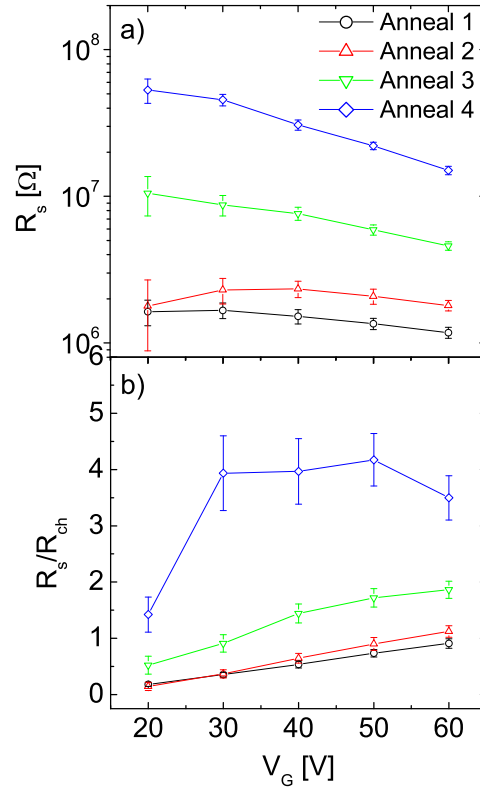
Figure 4.2: a) Gate voltage dependence of R_s for different anneals for the Au device at room temperature. b) R_s/R_{ch} as a function of V_G for a Au device with $L = 10\ \mu$m.

injection from Au and Pt for a certain dedoped level at $T = 300$ K and $V_G = -80$ V with $L = 7\ \mu$m and $W = 200\ \mu$m. Previous scanning potentiometry experiments [33, 34, 54] reveal that in systems with significant Δ most of the potential drop due to contacts occurs at the source. Fig. 4.3 is consistent with the the formation of a larger injection barrier between Au and P3HT than Pt under identical annealing conditions. Note that the lack of nonlinearity in Pt/P3HT/Pt (hole injection from Pt, hole collection by Pt) devices (see Fig. 4.1b) compared with the nonlinear data of Fig. 4.3 in the Au/P3HT/Pt (hole injection from Au, hole collection by Pt) configuration further supports the conclusion

that the *injecting* contact is the source of the nonlinearities.
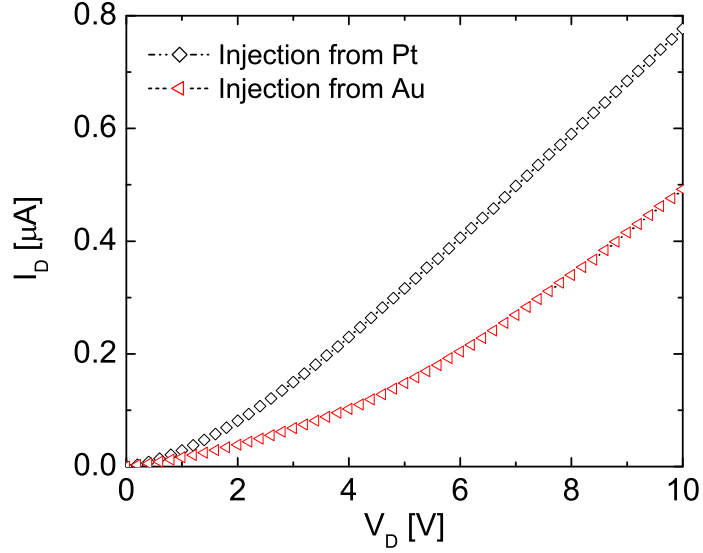
Figure 4.3: Linear plot of $I_D - V_D$ for injection from Au and Pt for a sample at 300 K and $V_G = -80$ V. This sample was dedoped such that bulk conductivity at 300 K was below our measurement threshold.

4.3.2 The spectroscopy results

Dopant concentration clearly affects charge transport across the interface between the OSC and injecting electrodes. Therefore examining the band alignment and interfacial dipole is imperative. Ultraviolet photoelectron spectroscopy (UPS) is a useful tool to monitor changes in valance electronic structure and work function of the interface. Previous studies of pentacene-based devices [67] have shown interface dipole formation at the metal/organic interface which varies linearly with the measured metal work function. Here, we show the results of the UPS study for Au/P3HT and Pt/P3HT interfaces.

Figure 4.4 shows the UPS cutoff of a P3HT/Au sample for different annealing times
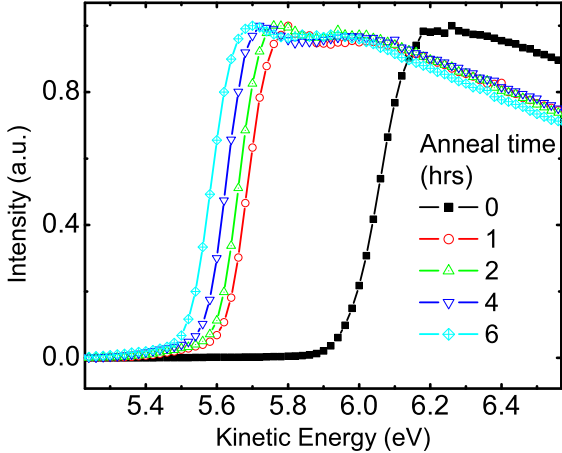
Figure 4.4: UPS cutoff of P3HT/Au sample for different annealing times at 350 K.

at 350 K. After 6 hours of annealing, the total change in the vacuum level, which appears as a series of shifts in the cutoff data, is about 0.5 eV. Fig. 4.5 plots the energy shift as a function of annealing time for both Au/P3HT and Pt/P3HT. The cutoff shift for Pt/P3HT after 5 hours is 0.2 eV. These shifts correspond to an increase in the Au/P3HT bulk valence level by these amounts. Fig. 4.6 shows the band alignment inferred from UPS for Au/P3HT before and after the annealing process. The appearance of 0.5 eV of additional hole injection barrier is consistent with increased contact resistance and nonlinear charge injection data shown in Fig. 4.1a. Since the energy shift for Pt/P3HT samples is smaller, less contact limitations are expected. This is consistent with observations in these devices. The difference between Au and Pt is likely related to their differing work functions and surface chemistries.

The UPS measurements and energy level diagrams of Figs. 4.4-4.6 do not directly probe the band alignment at the metal/organic interface, as the solution-cast P3HT
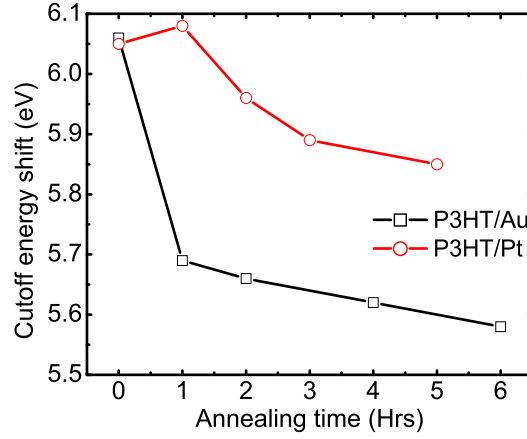
Figure 4.5: UPS cutoff energy shift as a function of annealing time for both P3HT/Au and P3HT/Pt.

layer is too thick to permit direct assessment of the metal/P3HT interface. Two effects difficult to discriminate in these samples may contribute to the changes in level alignment and injection mechanism with doping: band bending in the bulk, and surface dipole modification directly at the interface.

Band bending effects have been seen in an experiment [68] involving p-doping of zinc phthalocyanine, where Gao and Kahn have shown that in addition to the reduction of the interface dipole upon doping, the valence (highest occupied molecular orbital, HOMO) level shifts towards E_F within a layer thickness of a few nanometers. This shift indicates the formation of a space charge region and band bending near the interface. The improved transport at high doping levels in that experiment is associated with an increase in film conductivity, a decrease in barrier thickness as screening improves, and tunneling of carriers through the now-thin interface barrier.
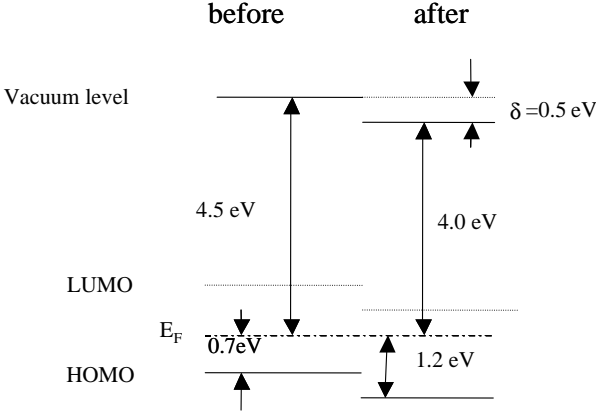
Figure 4.6: Energy level diagram of band alignment, based on the results of the UPS data for Au/P3HT before and after the annealing process, showing the large change in the barrier for hole injection.

The other possible contribution to the observed change in the injection barrier by annealing is the removal of the interface impurities, most likely H_2O. Heating inside vacuum can remove H_2O from the metal electrode surface, resulting in more direct contact of the organic with the electrode. The interface barrier in this case will be determined by the metal/organic interface dipole, and it will be smaller for Pt than for Au because of the higher workfunction of Pt [67]. The smaller barrier for Pt is also supported by the less change of the cutoff upon annealing as observed with UPS. Although the formation of a direct contact to metal will increase the barrier for both Pt and Au, the smaller value of the increase still allows Pt contact to be Ohmic. Once re-exposed to ambient conditions, impurities may diffuse back into the interface, resulting in a recovery of the injection properties of the un-annealed devices. The reduction of the hole injection barrier by ambient exposure of the metal electrode has recently been observed [69] in another OSC on Au by Wan et al.

We note, however, that the annealing processes used in this work are very mild compared to those typically used to remove physisorbed interfacial impurities such as water. Typical UHV baking procedures for desorption require temperatures considerably in excess of 370 K, while we observe significant effects even at 320 K. This suggests that desorption of interfacial impurities is unlikely to be the dominant source of the observed effects.

4.4 Conclusions

To examine the physics of charge injection from metals into disordered organic semiconductors, we examined transport properties of a series of organic FETs with P3HT as the active polymer layer and Pt and Au as the source/drain electrodes as a function of annealing and resulting dopant concentration. We extract the contact and channel resistances from the length dependence of the resistance, and observed that the contact resistance is dominant and strongly nonlinear at lower dopant concentrations and higher gate voltages for Au/P3HT samples. These effects are much less severe in Pt/P3HT samples. UPS data reveal that upon dedoping, the energy levels shift at the interface, leading to an increased barrier for hole injection. This shift is stronger for Au samples than Pt, consistent with strong nonlinear charge injection observed for Au samples at high dedopings. These results demonstrate that doping can profoundly affect the physics of charge injection in such systems by strongly altering the band alignment between the metal and the organic. The scale of the interface dipole shifts can significantly exceed the dopant-induced broadening of the density of states. Understanding such interfacial charge transfer and band alignment is essential to a complete description of metal/OSC

interfaces.

Chapter 5

CONTROLLING CHARGE INJECTION IN ORGANIC FIELD-EFFECT TRANSISTORS USING SELF-ASSEMBLED MONOLAYERS

5.1 Introduction

As mentioned previously, the electronic structure of the OSC/contacting electrode interface can strongly affect the overall performance of the OFET devices. The band alignment at the OSC/metal interface is influenced by several factors such as interfacial dipole formation [67, 70, 71], electrode contamination [69], and OSC doping [68, 72]. In Chapter 4, we examined the influence of impurity dopants on charge injection and band alignment at the metal/OSC interface in P3HT OFETs. Our results indicated that at lower dopant concentrations, an energetic realignment of bands occurs at the interface, leading to an increased barrier for hole injection. In addition, we showed that the onset of non-Ohmic transport at low doping is much more severe in devices with Au source and drain electrodes than Pt. We attributed this to the high work function of the Pt electrodes. Therefore, it appears that an important factor in determining the nature of charge injection (contact limited vs. bulk limited) in OFETs is controlling the work function of the injecting electrodes.

It has previously been shown [73, 74, 75, 76] that, by self-assembly of a layer of molecules with an intrinsic electric dipole moment, the work function of metal electrodes can be lowered or raised, affecting the size of the injection barrier at the metal/OSC

interface. While limited attempts have been made to use this approach to engineer contacts in OFETs [77, 78], considerably more effort has been dedicated to contacts in OLEDs [74, 75, 79] and modification of the OSC/dielectric interface [80, 81] in OFETs. In this chapter, using channels of varying length, we systematically examine the contact resistances and true channel mobility at various doping levels of bottom-contact P3HT OFETs with Au electrodes modified by self-assembly of dipolar molecular monolayers. We correlate the transport data with self-assembled monolayer (SAM) induced work function changes as measured by scanning potentiometry. In the case of electron-poor (work function-raising) SAMs, we show that contact resistances remain low compared to the channel resistance and the transistors show linear transport. These observations are consistent with the "pinning" of the local chemical potential at the interface at an energy favorable to hole injection, and contrast sharply with the strongly nonlinear injection observed at low doping levels in OFETs made with bare Au electrodes. Furthermore, devices with electrodes modified by electron rich (work function-lowering) SAMs show nonlinear transport and low currents at all hole doping levels, becoming increasingly nonlinear as dopant density is reduced. This is consistent with formation of an increased injection barrier for holes in such devices.

The dipolar molecules used in this experiment were synthesized by Jacob Ciszek and David Corley from Prof. James Tour's laboratory as an inter-departmental (Physics-Chemistry) collaboration. The details of the fabrication process can be found in an online supplemental material to the Nano. Lett. article published over the results. The information about this article is listed in Appendix 2.

5.2 Experimental Details

As usual, the OFETs are prepared in the bottom-contact configuration, with the same parameters and geometry described in section 4.2. All the devices are made with Au electrodes by electron beam evaporation of 2.5 nm of Ti followed by 25 nm of Au.

Prior to SAM assembly, the substrates were cleaned for 2 min in an oxygen plasma. They were then immersed for about 24 h in a 1:1 ethanol-chloroform solution of the desired molecule at a ~0.25 mg/mL concentration, prepared under nitrogen gas. Three types of molecules were used in this experiment: an electron poor fluorinated oligo(phenylene ethynylene) (F-OPE) (see Fig. 5.1 inset), and two electron-rich oligomers, OPE-NH$_2$ (Fig. 5.1 inset) and OPE-2(NH$_2$) (not shown, but similar to OPE-NH$_2$ with an additional amine group immediately adjacent to the first). These molecules self-assemble from the thioacetate through standard Au-thiol deprotection chemistry [82]. F-OPE molecules are electron poor and upon assembly boost the metal work function (*vide infra*), while the amine-terminated OPEs are electron rich and are expected to have the opposite effect.

To characterize the effect of the SAM molecules on the effective Au work function, we used a multi-mode atomic force microscope (AFM) in the surface potential mode [83] to measure the surface potential difference between the SAM treated and bare Au substrates. The procedure for carrying out these measurements is described in Appendix 1. While not suited to absolute measurements of work function, this method is useful for comparing relative differences in work function between differently treated surfaces. By comparing measured contact potentials of unmodified and SAM-coated Au films, we found that the F-OPE treated Au substrates exhibited an effective work function increased by ~0.9 eV

for an assembly period of two days relative to untreated co-evaporated Au films. In addition, the F-OPE treated samples showed stability and consistency in contact potential measurements over extended periods (days) of exposure to ambient conditions. For the OPE-NH$_2$ and OPE-2(NH$_2$) treated surfaces, however, it was difficult to obtain consistent surface potential differences with respect to bare Au, though most showed a slight decrease ($\sim$0.1 eV) in work function. These difficulties appear to result from instability of the resulting surfaces under extended exposure to ambient conditions. However, as shown below, these electron-rich molecules have a clear impact on band energetics at the interface, with transport measurements suggesting the formation of an injection barrier for holes.

After the SAM assembly, the P3HT solution, prepared as described in section 4.2, is solution cast onto the treated substrate, with the solvent allowed to evaporate in ambient conditions. The measurements are performed in vacuum ($\sim 10^{-6}$ Torr) in a variable temperature range probe station using a semiconductor parameter analyzer. As described in Chapter 4, the samples as prepared are highly doped and show a significant background ($V_\mathrm{G} = 0$) conduction. To reduce this impurity doping, the sample is annealed at elevated temperatures ($\sim$350-380 K) in vacuum for several hours and then cooled to room temperature for measurement. This results in a reduction in the background dopant concentration as easily characterized through the two-terminal bulk P3HT conductivity.

5.3   Results and Discussion

Figure 5.1a shows the transport characteristics of a Au/P3HT device with $L = 40$ μm at $T = 300$ K and at a fixed $V_\mathrm{G} = -70$ V for different doping levels. In anneal$_1$, the sample

was vacuum treated in the analysis chamber at 300 K for 16 h. Anneal$_2$ corresponds to the sample being further heated in vacuum for 18 h at 350 K, while anneal$_3$ includes yet an additional 18 h at 360 K. As in earlier experiments described in Chapter 4, the transport in this device with unmodified Au electrodes becomes nonlinear at high annealing steps, and the current drops by orders of magnitude. We attributed this to the formation of an increased injection barrier for holes, and similar effects have been reported by others [64].
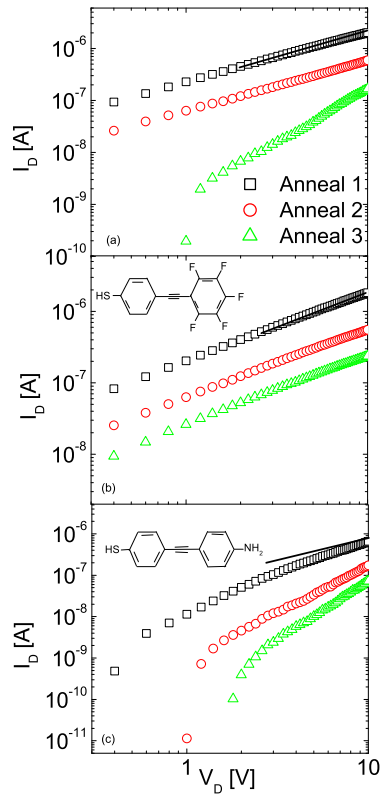
Figure 5.1: a) A log-log plot of the transport characteristics of a Au/P3HT device for different annealing as described in the text. b) Similar plot for a Au/P3HT device with the electrodes modified by F-OPE SAM shown in the inset. c) Au/P3HT device with electrodes modified by OPE-NH$_2$ SAM molecules shown in the inset. For all devices, $L = 40$ μm at $T = 300$ K and at a fixed $V_G = -70$ V with the same annealing schedule. The solid black line has a slope of 1.

In contrast, Fig. 5.1b shows the transport for a device with similar geometric parameters and annealing schedule, in which the electrodes were modified by F-OPE SAM molecules prior to P3HT deposition. Even though I_D drops at higher annealing steps, the currents remain linear with V_D and as shown below, the contact resistance remains much lower compared to bare Au devices. This behavior is similar to our previous observations (Chapter 4) for Pt/P3HT devices. These effects have been verified in annealing cycles on multiple arrays of F-OPE treated devices.

In Fig. 5.1c, the electrode surfaces were modified by OPE-NH$_2$. In this case, the currents are much lower than in either (a) or (b), and even when the hole doping of the P3HT is significant, injection is non-Ohmic, with I_D rising super-linearly with V_D. In highly annealed conditions, this behavior is super-quadratic. Transport data for the OPE-2(NH$_2$) treated devices qualitatively looks very similar to those in Fig. 5.1c.

From the data in Figs. 5.1a and 5.1b, we extract the channel resistance, R_{ch}, the intrinsic device mobility, μ, and the contact resistance R_s from the L dependence of the total device resistance, $R_{on} \equiv \partial V_D/\partial I_D$ over a T and V_G range as described in section 3.2. We obtain R_s in the limit $|V_D| < 1V$, where transport is still reasonably linear even after the longer annealing runs. We note that while we have developed a procedure for extracting contact current-voltage characteristics even in the limit of strong injection nonlinearities (section 3.3), it is difficult to quantify such injection by a single number such as R_s. In the shallow channel limit, it is straightforward to convert the gate dependence of R_{ch} into a field-effect mobility.

Figure 5.2 shows a log-log plot of μ vs R_s for two sets of devices over a series of temperatures and gate voltages for an initial annealing step. The open symbols correspond

to data from the F-OPE treated electrodes and the filled symbols are extracted from bare Au/P3HT data. The error bars come from the uncertainty in the slope and intercept of R_{on} vs. L plots. Indeed, in device arrays with $R_{\mathrm{s}} << R_{\mathrm{ch}}$, deviations from perfect scaling of $R_{\mathrm{ch}} \propto L$ can lead to "best fit" values of R_{s} that are actually negative (and hence cannot be plotted on such a figure), though with appropriately large error bars. Here, the mobility and the contact resistance for both device sets are similar, consistent with similarity in the magnitude of $I_{\mathrm{D}} - V_{\mathrm{D}}$ for both samples. In the proceeding annealing steps, however, the contact resistance for the sample with untreated electrodes increases significantly, compared to the SAM treated device (Figs. 5.2b and (c)). Whereas the Au/P3HT devices become severely contact limited at high dedopings, the treatment of Au electrodes with F-OPE molecules keeps the contact resistance relatively low compared to channel resistance, and the transport characteristics remain *linear*. This Ohmic injection persists even when bulk $V_{\mathrm{G}} = 0$ conduction in the P3HT film is completely suppressed at room temperature.

Our results in F-OPE treated devices are quantitatively similar to those obtained in charge injection from Pt electrodes into P3HT as outlined in Chapter 4. Although it is difficult to probe the energy level alignment directly at the metal/organic interface (due to the the thick P3HT film resulting from solution casting), it is clear that increasing the Au effective work function results in improved electronic performance of these OFETs. In light of the many experiments showing the formation of interfacial dipoles at the metal/OSC interface upon deposition of the OSC [67, 70, 71], it is possible that introduction of work function-raising SAMs such as F-OPE in our experiments counteracts or prevents the work function-lowering effect of these interfacial dipoles. This can result in a
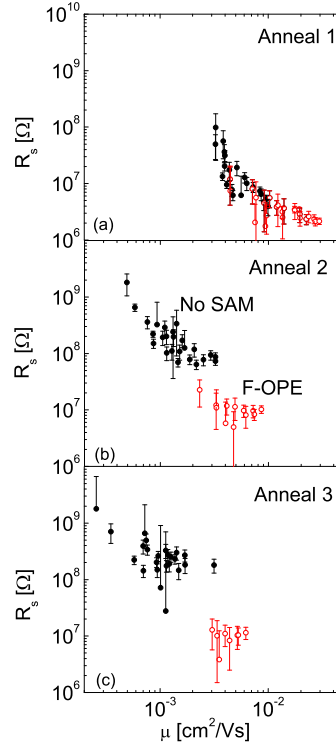
Figure 5.2: a) A log-log plot of μ vs R_s for 2 sets of devices over a series of temperatures and gate voltages. The open symbols correspond to data from the F-OPE treated electrodes and the filled symbols are extracted from bare Au/P3HT data. Anneal$_1$ here corresponds to sample being pumped on in vacuum at 320 K overnight. b) data retaken after sampled was annealed at 350 K for 18 h (anneal$_2$). c) data taken again after another anneal step similar to (b). The reason for fewer data points in parts (b) and (c) for SAM treated sample is a smaller contact resistance with significant error compared to the channel resistance.

pinning of the energy levels at the interface such that there is a small or non-existent injection barrier for holes. On the other hand, the work function-lowering OPE-NH$_2$ SAMs appear to contribute more substantially to the interfacial dipoles, resulting in significant Schottky barrier formation for holes at the interface and severe nonlinear injection in these devices. The subsequent dedopings have the same implications discussed in the previous chapter.

One must also consider whether the different injection properties could result from SAM-induced changes in the ordering of the P3HT at the metal-OSC interface. Such morphological differences may occur, and would require careful interface-sensitive spectroscopies or scattering measurements to confirm. However, while improved P3HT ordering at the F-OPE/P3HT interface would result in higher mobilities and lower contact resistances, we find it unlikely that morphological changes alone could explain the dramatic difference in injection properties as a function of doping. The data in Fig. 5.2 strongly suggest significant differences in the band energetics between the F-OPE treated and untreated Au electrodes.

5.4   Conclusions

We have used dipole-containing self-assembled monolayers on the Au source and drain electrodes to strongly manipulate the charge injection process across the metal-organic interface in a series of polymer FETs based on P3HT. To see the effect of dopant concentration on device performance, we measure device properties after each of a series of mild annealing steps in vacuum. We extract the contact resistances and the intrinsic channel mobility from the length dependence of the resistance for bare Au/P3HT and flourinated-OPE Au/P3HT devices where transport is still relatively linear at low drain bias. At low dopant concentrations, SAM-modified devices show significantly lower contact resistances and higher mobilities compared to unmodified devices. We attribute these findings to higher metal work function and small injection barriers for holes in the case of F-OPE SAM modified devices, resulting from better energetic alignment with the valence band of the organic semiconductor. These results quantitatively demonstrate

the power of simple surface chemistry in modifying the dynamics of charge at interfaces with OSCs, even in nearly undoped material. Such techniques will be generally useful in significantly improving technologies based on these versatile materials.

Chapter 6

FINAL REMARKS AND FUTURE DIRECTION

In this thesis, we investigated a series of outstanding problems related to charge injection and transport in organic field-effect transistors. This is a relatively new area and more work needs to be done in way of understanding the nature of charge transport in these devices. I am very honored and pleased to have contributed to the growth of this field through our experiments and analyses and under the guidance of my advisor and by many contributions from our collaborators.

Our results of linear charge injection from Au electrodes into P3HT, for example, demonstrated that contact resistivity and the true channel mobility are closely related and models of charge injection should address this relationship. For the nonlinear data analysis from metals with low work functions, we developed a technique of extracting the contact current-voltage characteristics from the transport data by using the scaling of the current with channel length. This data was then compared with the predictions of a recent hopping injection model with emphasis on the primary injection event. We showed that an energy-dependent disordered density of localized states in the organic semiconductor seems to be an important factor for the weak temperature dependence of the currents observed in our transistor devices. This indicates that diffusion-limited models are not entirely reliable.

However, there are several unaddressed issues in our analysis of the nonlinear data. The most interesting is the presence of small depletion regions formed in the vicinity of

the contacts. The size of these region, the charge carrier density and mobility and the gate voltage dependence of the current are all important issues that need to be investigated in detail. Improved local probes, such as high resolution scanning potentiometry or scanning tunneling microscopy, would be extremely useful in better understanding these depletion regions. Also, more theoretical work and modeling on the nature of these regions are essential. One experiment that can be performed here at Rice as a continuation of this work is fabrication of small gaps on the order of 100 nm and below followed by extensive measurements of device characteristics as a function of temperature and the gate voltage. At such length scales, the transistor channel made from low work function contact metals is expected to comprise partially or entirely of a depletion region. By fabricating devices with various metals and measuring the transport at different annealing steps, we expect to gain valuable information about the operation of the device in this regime.

The ultimate goal of this proposed experiment, however, is to fabricate devices with small enough gaps ($\sim$ 10 nm) that could allow us to measure transport through single polymer chains. In this case, the charge carriers should move along the polymer chain and not be limited by inter-chain hopping. Therefore, we expect to observe a band-like transport. The mobility should remain the same or even improve, as temperature is lowered. This is a complete diversion from the current trend in almost all organic semiconducting devices and has the potential to be a ground-breaking work.

Fabricating nanogaps also allows for transport studies in the regime of extremely high electric fields without using high operating voltages. In light of a recent work [84], suggesting voltage-induced metal-insulator transition in polythiophene transistors at high gate and source-drain voltages, this can be an interesting experiment to examine whether

this is a result of a true transition or is simply due to a temperature-independent process such as tunneling of carriers between localized states.

We also performed several experiments investigating the influence of dopants and work function fluctuations (through self-assembly of monolayers) on band alignment at the metal/organic semiconductor interface. The doping experiments revealed that at lower dopant concentrations, the size of the hole injection barrier between the organic semiconductor and the Fermi level of the metal increases. This naturally affects the nature of charge injection, making the contact resistances between the metal and the polymer nonlinear at low impurity concentrations. Self-assembly of SAMs on Au surfaces proved to be a more effective way of controlling injection barriers between the metal and the polymer. This technique can be used to systematically engineer these energy barriers and carefully study the effect of band alignment on charge injection in transistors.

Organic electronic materials and devices constitute a novel and exciting field and show great potential for commercial applications in the near future. Understanding the physics of operation in these devices is just as rewarding as developing new materials and device designs. In fact, this understanding is essential for the progress of the field and the application of these devices. The primary goal of this thesis has been precisely this: To contribute and enhance our understanding of the nature of charge transport in organic electronic devices. The results of our experiments have placed us among important contributors to this field and this work will continue along new directions in the future.

References

[1] C. DeBoer. *Organic LED Displays (OLEDs) − The Next Trend* ?, available at http://www.audioholics.com/techtips/specsformats/organicOLEDsdisplays.php.

[2] The top 3 polymer sketches are taken from: http://www.chem.sc.edu, 6T molecule sketch is available from http://www.sigmaaldrich.com, and the bottom sketch, pentacene is obtained from http://www.organicsemiconductor.com.

[3] G. Horowitz, "Organic thin film transistors: From theory to real devices," *J. Mater. Res.*, vol. 19, pp. 1946–1962, 2004.

[4] F. Gutmann and L. E. Lyons, *Organic Semiconductors.* John Wiley & Sons, Inc, 1967.

[5] W. F. Pasveer, *Charge and Energy Transport in Disordered π-conjugated Systems.* PhD thesis, Technische Universiteit Eindhoven, 2004.

[6] F. Garnier, "Scope and limits of organic-based thin-film transistors," *Phil. Trans.*, vol. 355, pp. 815–827, 1997.

[7] J. M. Shaw and P. F. Seidler, "Organic electronics: Introduction," *IBM J. Res. Dev.*, vol. 45, pp. 3–9, 2001.

[8] C. D. Dimitrakopoulos and D. J. Mascaro, "Organic thin-film transistors, a review of recent advances," *IBM J. Res. Dev.*, vol. 45, pp. 11–27, 2001.

[9] E. Cantatore, "Organic materials: A new chance for electronics?," *Proc. of the SAFE/IEEE workshop*, vol. workshop27, pp. 27–31, 2000.

[10] H. Sirringhaus, "Device physics of solution processed organic field-effect transistors," *Adv. Mat.*, vol. 17, pp. 2411–2425, 2005.

[11] M. C. J. M. Vissenberg, *Opto-Electronic Properties of Disordered Organic Semiconductors.* PhD thesis, 1999.

[12] M. Shur, *Physics of Semiconductor Devices.* Prentice Hall, Englewood Cliffs, 1990.

[13] M. Shur and M. Hack, "Physics of amorphous silicon based alloy field effect transistors," *J. Appl. Phys.*, vol. 55, pp. 3831–3842, 1984.

[14] R. A. Street and A. Salleo, "Contact effects in polymer transistors," *Appl. Phys. Lett.*, vol. 81, pp. 2887–2889, 2002.

[15] E. J. Meijer, D. M. D. Leeuw, S. Setayesh, E. van Veenendaal, B.-H. Huisman, P. W. M. Blom, J. C. Hummelen, U. Scherf, and T. M. Klapwijk, "Solution-processed ambipolar organic field-effect transistors and inverters," *Nat. Mater.*, vol. 2, pp. 678–682, 2003.

[16] T. Anthopoulos, C. Tanase, S. Setayesh, E. J. Meijer, J. C. Hummelen, P. W. M. Blom, and D. M. D. Leeuw, "Ambipolar organic field-effect transistors based on solution processed methanofullerene," *Adv. Mater.*, vol. 16, pp. 2174–2179, 2004.

[17] E. J. Meijer, C. Detcheverry, P. J. Baesjou, E. van Veenendaal, D. M. de Leeuw, and T. M. Klapwijk, "Dopant density determination in disordered organic field-effect transistors," *J. Appl. Phys.*, vol. 93, pp. 4831–4835, 2003.

[18] Z. Chiguvare, J. Parisi, and V. Dyakonov, "Current limiting mechanisms in indium-tin-oxide/poly3-hexylthiophene/aluminum thin film devices," *J. Appl. Phys.*, vol. 94, pp. 2440–2448, 2003.

[19] Y. Shen and G. G. Malliaras, "Charge injection into organic semiconductors," *The Spectrum*, vol. 13, pp. 1–4, 2000.

[20] P. N. Murgatroyd, "Theory of space-charge-limited current enhanced by frenkel effect," *J. Phys. D.*, vol. 3, pp. 151–156, 1970.

[21] W. D. Gill, "Drift mobilities in amorphous charge-transfer complexes of trinitrofluorenone and poly-n-vinylcarbazole," *J. Appl. Phys.*, vol. 43, pp. 5033–5040, 1972.

[22] P. W. M. Blom, M. J. M. de Jong, and M. G. van Munster, "Electric-field and temperature dependence of the hole mobility in poly(p-phenylene vinylene)," *Phys. Rev. B.*, vol. 55, pp. 656–659, 1997.

[23] M. C. J. M. Vissenberg and M. Matters, "Theory of the field-effect mobility in amorphous organic transistors," *Phys. Rev. B.*, vol. 57, pp. 12964–12967, 1998.

[24] J. C. Scott, "Metal-organic interface and charge injection in organic electronic devices," *J. Vac. Sci. Technol. A.*, vol. 21, pp. 521–531, 2003.

[25] P. R. Emtage and J. J. O'Dwyer, "Richardson-schottky effect in insulators," *Phys. Rev. Lett.*, vol. 16, pp. 356–358, 1966.

[26] V. Arkhipov, E. Emelianova, Y. Tak, , and H. Bässler., "Charge injection into light-emitting diodes: Theory and experiment," *J. Appl. Phys*, vol. 84, pp. 848–856, 1998.

[27] H. Böttger and V. Bryskin, *Hopping Conduction in Solids*. Akademie-Verlag, 1985.

[28] P. E. Parris, V. M. Kenkre, and D. H. Dunlap, "Nature of charge carriers in disordered molecular solids: are polarons compatible with observations?," *Phys. Rev. Lett.*, vol. 87, pp. 126601–126605, 2001.

[29] A. R. Brown, C. P. Jarrett, D. M. de Leeuw, and M. Matters, "Field-effect transistors made from solution-processed organic semiconductors," *Synth. Met.*, vol. 88, pp. 37–55, 1997.

[30] A. N. Aleshin, H. Sandberg, and H. Stubb, "Two-dimensional charge carrier mobility studies of regioregular p3ht," *Synth. Met.*, vol. 121, pp. 1449–1450, 2001.

[31] C. D. Dimitrakopoulos, S. Purushothaman, J. Kymissis, A. Callegari, and J. Shaw, "Low-voltage organic transistors on plastic comprising high-dielectric constant gate insulators," *Science*, vol. 283, pp. 822–824, 1999.

[32] G. Horowitz, R. Hajlaoui, D. Fichou, and A. E. Kassmi, "Gate voltage dependent mobility of oligothiophene field-effect transistors," *J. Appl. Phys.*, vol. 85, pp. 3202–3206, 1999.

[33] K. Seshadri and C. Frisbie, "Potentiometry of an operating organic semiconductor field-effect transistor," *Appl. Phys. Lett.*, vol. 78, pp. 993–995, 2001.

[34] L. Bürgi, H. Sirringhaus, and R. Friend, "Noncontact potentiometry of polymer field-effect transistors," *Appl. Phys. Lett.*, vol. 80, pp. 2913–2915, 2002.

[35] H. Klauk, G. Schmid, W. Radlik, W. Weber, L. Zhou, C. D. Sheraw, J. A. Nichols, and T. N. Jackson, "Contact resistance in organic thin film transistors," *Solid-State Electon.*, vol. 47, pp. 297–301, 2003.

[36] P. V. Necludiov, M. S. Shur, D. Gundlach, and T. N. Jackson, "Contact resistance extraction in pentacene thin film transistors," *Solid-State Electon.*, vol. 47, pp. 259–262, 2003.

[37] J. Zaumseil, K. Baldwin, and J. Rogers, "Contact resistance in organic transistors that use source and drain electrodes formed by soft contact lamination," *J. Appl. Phys.*, vol. 93, pp. 6117–6124, 2003.

[38] E. Meijer, G. Gelinck, E. van Veenendaal, B.-H.Huisman, D. de Leeuw, and T. Klapwijk, "Scaling behavior and parasitic series resistance in disordered organic field-effect transistors," *Appl. Phys. Lett.*, vol. 82, pp. 4576–4578, 2003.

[39] Sigma-Aldrich Inc., St. Louis, MO.

[40] Z. Bao, A. Dodabalapur, and A. Lovinger, "Soluble and processable regioregular poly(3-hexylthiophene) for thin film field-effect transistor applications with high mobility," *Appl. Phys. Lett.*, vol. 69, pp. 4108–4110, 1996.

[41] H. Sirringhaus, N. Tessler, and R. H. Friend, "Integrated optoelectronic devices based on conjugated polymers," *Science*, vol. 280, pp. 1741–1744, 1998.

[42] H. S. et al, "Two-dimensional charge transport in self-organized, high-mobility conjugated polymers," *Nature (London)*, vol. 401, pp. 685–688, 1999.

[43] E. J. M. et al., "Switch-on voltage in disordered organic field-effect transistors," *Appl. Phys. Lett.*, vol. 80, pp. 3838–3840, 2002.

[44] G. G. Malliaras, J. R. Salem, P. J. Brock, and C. Scott, "Electrical characteristics and efficiency of single-layer organic light-emitting diodes," *Phys. Rev. B*, vol. 58, pp. R13411–R13414, 1998.

[45] M. Austin and S. Chou, "Fabrication of 70 nm channel length polymer organic thin-film transistors using nanoimprint lithography," *Appl. Phys. Lett.*, vol. 81, pp. 4431–4433, 2002.

[46] M. A. Alam, A. Dodabalapur, and M. R. Pinto, "A two-dimensional simulation of organic transistors," *IEEE Trans. Electon Devices*, vol. 44, pp. 1332–1337, 1997.

[47] S. V. Novikov, D. H. Dunlap, V. M. Kenkre, P. Parris, and A. V. Vannikov, "Essential role of correlations in governing charge transport in disordered organic materials," *Phys. Rev. Lett.*, vol. 81, pp. 4472–4475, 1998.

[48] S. Rakhmanova and E. Conwell, "Electric-field dependence of mobility in conjugated polymer films," *Appl. Phys. Lett.*, vol. 76, pp. 3822–3824, 2000.

[49] T. van Woudenbergh, P. W. M. Blom, M. C. M. Vissenberg, and J. Huiberts, "Temperature dependence of the charge injection in poly-dialkoxy-p-phenylene vinylene," *Appl. Phys. Lett.*, vol. 79, pp. 1697–1699, 2001.

[50] P. V. Pesavento, R. J. Chesterfield, C. R. Newman, and C. D. Frisbie, "Gated four-probe measurements on pentacene thin-film transistors: Contact resistance as a function of gate voltage and temperature," *J. Appl. Phys.*, vol. 96, pp. 7312–7324, 2004.

[51] M. Abkowitz, S. Facci, and J. Rehm, "Direct evaluation of contact injection efficiency into small molecule based transport layers: Influence of extrinsic factors," *J. Appl. Phys*, vol. 83, pp. 2670–2676, 1998.

[52] J. C. Scott and G. G. Malliaras, "Charge injection and recombination at the metal-organic interface," *Chem. Phys. Lett.*, vol. 299, pp. 115–119, 1999.

[53] Y. Shen, M. W. Klein, D. B. Jacobs, J. C. Scott, and G. G. Malliaras, "Mobility-dependent charge injection into an organic semiconductor," *Phys. Rev. Lett.*, vol. 86, pp. 3867–3870, 2001.

[54] L. Bürgi, T. J. Richards, R. H. Friend, and H. Sirringhaus, "Close look at charge carrier injection in polymer field-effect transistors," *J. Appl. Phys.*, vol. 94, pp. 6129–6137, 2003.

[55] S. F. Nelson, Y.-Y. Lin, D. J. Gundlach, and T. N. Jackson, "Temperature-independent transport in high-mobility pentacene transistors," *Appl. Phys. Lett.*, vol. 72, pp. 1854–1856, 1998.

[56] J. Reynaert, V. I. Arkhipov, G. Borghs, and P. Heremans, "Currentvoltage characteristics of a tetracene crystal: Space charge or injection limited conductivity?," *Appl. Phys. Lett.*, vol. 85, pp. 603–605, 2004.

[57] V. I. Arkhipov, U. Wolf, and H. Bässler, "Current injection from a metal to a disordered hopping system. ii. comparison between analytic theory and simulation," *Phys. Rev. B.*, vol. 59, pp. 7514–7520, 1999.

[58] T. Li, P. P. Ruden, I. H. Campbell, and D. L. Smith, "Investigation of bottom-contact organic field effect transistors by two-dimensional device modeling," *J. Appl. Phys.*, vol. 93, pp. 4017–4022, 2003.

[59] H. C. F. Martens, P. W. M. Blom, and H. F. M. Schoo, "Comparative study of hole transport in poly(p-phenylene vinylene) derivatives," *Phys. Rev. B.*, vol. 61, pp. 7489–7493, 2000.

[60] H. Bässler, "Charge transport in disordered organic photoconductors a monte carlo simulation study," *Phys. Stat. Sol. B*, vol. 175, pp. 15–56, 1993.

[61] I. G. Hill, A. Rajagopal, A. Kahn, and Y. Hu, "Molecular level alignment at organic semiconductor-metal interfaces," *Appl. Phys. Lett.*, vol. 73, pp. 662–664, 1998.

[62] X. Crispin, V. Geskin, A. Crispin, J. Comil, R. Lazzaroni, W. Salaneck, and J.-L. Brédas, "Characterization of the interface dipole at organic/metal interfaces," *J. Am. Chem. Soc.*, vol. 124, pp. 8131–8141, 2002.

[63] N. Koch, A. Kahn, J. Ghijsen, J.-J. Pireaux, J. Schwartz, R. Johnson, and A. Eischner, "Conjugated organic molecules on metal versus polymer electrodes: Demonstration of a key energy level alignment mechanism," *Appl. Phys. Lett.*, vol. 82, pp. 70–72, 2003.

[64] D. B. A. Rep, A. F. Morpurgo, and T. M. Klapwijk, "Doping-dependent charge injection into regioregular poly(3-hexylthiophene)," *Org. Electron.*, vol. 4, pp. 201–207, 2003.

[65] A. R. Hosseini, M. H. Wong, Y. Shen, and G. G. Malliaras, "Charge injection in doped organic semiconductors," *J. Appl. Phys.*, vol. 97, pp. 023705–1, 2005.

[66] S. Hoshino, M. Yoshida, S. Uemura, T. Kodzasa, N. Takada, T. Kamata, and K. Yase, "Influence of moisture on device characteristics of polythiophene-based field-effect transistors," *J. Appl. Phys.*, vol. 95, pp. 5088–5093, 2004.

[67] N. J. Watkins, L. Yan, and Y. Gao, "Electronic structure symmetry of interfaces between pentacene and metals," *Appl. Phys. Lett.*, vol. 80, pp. 4384–4386, 2002.

[68] W. Gao and A. Kahn, "Controlled p-doping of zinc phthalocyanine by coevaporation with tetrafluorotetracyanoquinodimethane: A direct and inverse photoemission study," *Appl. Phys. Lett.*, vol. 79, pp. 4040–4042, 2001.

[69] A. Wan, J. Hwang, F. Amy, and A. Kahn, "Impact of electrode contamination on the a-npd/au hole injection barrier," *Org. Electron.*, vol. 6, pp. 47–54, 2005.

[70] M. Knupfer and G. Paasch, "Origin of the interface dipole at interfaces between undoped organic semiconductors and metals," *J. Vac. Sci. Technol. A*, vol. 23, pp. 1072–1077, 2005.

[71] H. Ishii, K. Sugiyama, E. Ito, and K. Seki, "Energy level alignment and interfacial electronic structures at organic/metal and organic/organic interfaces," *Adv. Mater.*, vol. 11, pp. 605–625, 1999.

[72] W. Gao and A. Kahn, "Controlled p doping of the hole-transport molecular material n,n-diphenyl-n,n-bis(1-naphthyl)-1,1-biphenyl-4,4-diamine with tetrafluorotetracyanoquinodimethane," *J. Appl. Phys.*, vol. 94, pp. 359–366, 2003.

[73] I. H. Campbell, S. Rubin, T. A. Zawodzinski, J. D. Kress, R. L. Martin, D. L. Smith, N. N. Barashkov, and J. P. Ferraris, "Controlling schottky energy barriers in organic electronic devices using self-assembled monolayers," *Phys. Rev. B.*, vol. 54, pp. R14321–R14324, 1996.

[74] F. Nüesch, F. Rotzinger, L. Si-Ahmed, and L. Zuppiroli, "Chemical potential shifts at organic device electrodes induced by grafted monolayers," *Chem. Phys. Lett.*, vol. 288, pp. 861–867, 1998.

[75] L. Zuppiroli, L. Si-Ahmed, K. Kamaras, F. Nüesch, M. N. Bussac, D. Ades, A. Siove, E. Moons, and M. Grätzel, "Chemical potential shifts at organic device electrodes induced by grafted monolayers," *Eur. Phys. J. B*, vol. 11, pp. 505–512, 1999.

[76] J. M. Tour, A. M. Rawlett, M. Kozaki, Y. Yao, R. C. Jagessar, S. M. Dirk, D. W. Price, M. A. Reed, C. Zhou, J. Chen, W. Wang, and I. Campbell, "Synthesis and preliminary testing of molecular wires and devices," *Chem-Eur. J.*, vol. 11, pp. 5118–5134, 2001.

[77] D. J. Gundlach, L. Jia, and T. N. Jackson, "Pentacene tft with improved linear region characteristics using chemically modified source and drain electrodes," *IEEE Electron Device Lett.*, vol. 22, pp. 571–573, 2001.

[78] S. H. Kim, J. H. Lee, S. C. Lim, Y. S. Yang, and T. Zyung, "Improved contact properties for organic thin-film transistors using self-assembled monolayer," *Jpn. J. Appl. Phys.*, vol. 43, pp. L60–L62, 2003.

[79] B. de Boer, A. Hadipour, M. M. Mandoc, T. van Woudenbergh, and P. W. M. Blom, "Tuning of metal work functions with self-assembled monolayers," *Adv. Mater.*, vol. 17, pp. 621–625, 2005.

[80] K. P. Pernstich, S. Haas, D. Oberhoff, C. Goldmann, D. J. Gundlach, B. Batlogg, A. N. Rashid, and G. Schitter, "Threshold voltage shift in organic field effect transistors by dipole monolayers on the gate insulator," *J. Appl. Phys.*, vol. 96, pp. 6431–6438, 2004.

[81] R. J. Kline, M. D. McGehee, and M. F. Toney, "Highly oriented crystals at the buried interface in polythiophene thin-film transistors," *Nat. Mater.*, vol. 5, pp. 222–228, 2006.

[82] L. Cai, Y. Yao, J. Yang, D. W. P. Jr., and J. M. Tour, "Chemical and potential-assisted assembly of thiolacetyl-terminated oligo(phenylene ethynylene)s on gold surfaces," *Chem. Mater.*, vol. 14, pp. 2905–2909, 2002.

[83] Surface Potential Detection Manual, Veeco Inst. Sec. 231.6.

[84] A. S. Dhoot, G. M. Wang, D. Moses, and A. J. Heeger, "Voltage-induced metal-insulator transition in polythiophene field-effect transistors," *Phys. Rev. Lett*, vol. 96, p. 246403, 2006.

Appendix A

A Guide to Surface Potential Measurements

The work function changes between SAM treated and bare Au substrates described in Chapter 5 were measured by South AFM, located in the Shared Equipment room in Dell Butcher hall. This is a Multimode AFM with an Extender Electronic Module suited for surface potential measurements. The technique is a two-pass process, where in the first pass, the topography of the sample is mapped and on the second pass, the potential profile is measured. The surface potential manual (Ref. 83) does a really good job of explaining the background theory and laying out the procedure to do this measurement. However, here I add this complimentary section to help make the use of this instrument more straightforward. I will assume that the reader is familiar with the operation of the AFM.

The sample under study should be conductive and should make good contact to the AFM specimen disc by using a conductive epoxy, such as silver paint. This ensures that the sample makes good electrical contact to the ground. Also, this allows a voltage to be applied to the sample through the carefully modified jumper configuration at the bottom of the unit. The BNC cable attached to the bottom of the AFM is for this purpose. Normally, it is grounded but the grounding cap can be removed and the cable can be hooked to a power supply. Avoid sourcing too much current to the specimen; probably less than 1 μA is a good number. Increase the applied voltage in increments of 100 mV.

For the tip, use MESP or SCM-PIT type which are conductive and have a relatively low resonant frequency ($\sim$60-80 kHz). Notice that length-wise, they are much longer than normal Si tips and they are extremely expensive ($80 per tip), so please handle them with care. You also have to use the special EFM tip holder in order for this measurement to work. As of now, we have only one and since one of the normal tip holders is broken, the EFM holder is also being used for normal AFM operations. There are 2 ways you can tell it apart from the normal holder. The easy way is to look directly at the screw that holds the clip going over the tip. If you see a white teflan washer underneath it, then

you have the EFM tip holder in your hand. The Teflan keeps the tip electrically isolated from the surrounding. The second way is, of course, to check whether the clip is isolated from the rest of the holder by using a digital multimeter.

Remember that everything in this measurement is relative, and you cannot expect to get absolute values for work functions or surface potential of your samples. Typically, the way I perform the experiment is to first place my bare-Au samples on the piezo, optimize the AFM for imaging and then start the surface potential measurement and measure the average value of the surface voltage in absolute numbers, then I would simply stop the operation by lifting the cantilever, carefully unscrew the holder, pull the sample straight out and place the Au-treated sample on the piezo, and repeat the measurement. The difference in the average values of the surface potentials measured represents the effective change in work function between the two samples.

Follow these guidelines to perform your measurements. They were provided to me by Veeco technicians (John Tedesco, jtedesco@veeco.com):

1. After securing your sample and the tip holder, make sure the switches on the extender box are set to Surface Potential and GND/Surface Potential.

2. On channel 1, set Line direction=Retrace, Scan line=Main, Real planefit=Line and Offline planefit=Full, run the AFM in normal mode and obtain a good height profile image.

3. Open Other Controls panel, set igain=10 and pgain=100 as starting values

4. Open the Interleaves Controls panel. Use Input feedback=potential, Drive amplitude=6000 mV, Drive phase=-90^0, Interleave mode=Lift and Lift scan height=0 nm. If there is button in front of any of these values, it should be turned on to green. All other parameters can be left grey.

5. Finally on channel 2, set Data type=Potential, Line direction=Retrace, Scan line=Interleave and Realtime planefit and Offline planefit to None. This is important if you want to compare absolute values only (as in my measurements). If you are interested in the surface potential profile of the surface only, then you can average it by a linefit. To see the absolute values, it's easier to switch to the Scope Mode and set the scale appropriately to read the numbers. The Scope Mode button is located on top of the normal screen. You can use the capture button to take snapshots of the scope screen.

The above settings should work for most cases. If the measurement seems to work, but the signal is not stable, try playing around with the gains and/or the drive phase and amplitude. Remember also that it's essential for the height scan data to be going well. If the optical image is not good, the surface potential can be affected. Also consider changing your tip every so often, as in normal AFM. If nothing seems to work right, you can try to get help from Veeco.

Appendix B

List of Publications

B. H. Hamadani, D. Corley, J. Ciszek, J. M. Tour and D. Natelson, "Controlling charge injection in organic field-effect transistors using self-assembled monolayers". Nano Lett. 6, 1303 (2006).

B. H. Hamadani, H. Ding, Y. Gao, and D. Natelson, "Doping dependent charge injection and band alignment in organic field effect transistors". Phys. Rev. B. 72, 235302 (2005).

B. H. Hamadani and D. Natelson, "Nonlinear charge injection in organic field effect transistors". J. Appl. Phys. 97, 064508 (2005).

B. H. Hamadani and D. Natelson, "Extracting contact effects in OFETs". Proc. IEEE. 93, 1306 (2005).

B. H. Hamadani and D. Natelson, "Temperature dependent contact resistances in high quality polymer field effect transistors". Appl. Phys. Lett. 84, 443 (2004).

B. H. Hamadani and D. Natelson, "Gated nonlinear transport in organic polymer field effect transistors". J. Appl. Phys. 95, 1227 (2004).

B. H. Hamadani and D. Natelson, "Gated nonlinear transport in organic thin film transistors". Mat. Res. Soc. Symp. Proc. 771, 187 (2003).